MOUNTAIN-PLAINS CONSORTIUM

MPC 15-282 | M. Yang

An Integrated Real-Time Health Monitoring and Impact/Collision Detection System for Bridges in Cold Remote Regions

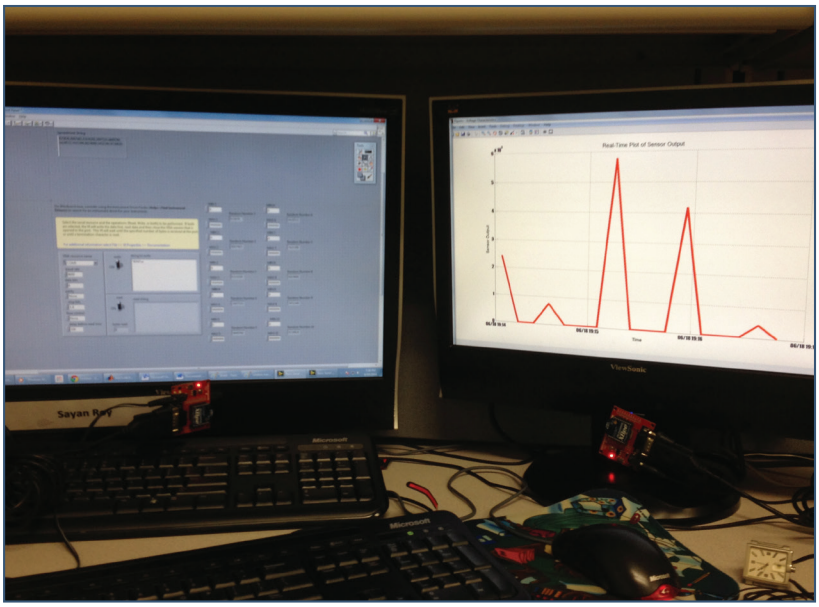

MPC
MOUNTAIN-PLAINS CONSORTIUM

A University Transportation Center sponsored by the U.S. Department of Transportation serving the Mountain-Plains Region. Consortium members:

Colorado State University
North Dakota State University
South Dakota State University
University of Colorado Denver
University of Denver
University of Utah
Utah State University
University of Wyoming

An Integrated Real-Time Health Monitoring and Impact/Collision Detection System for Bridges in Cold Remote Regions

Mijia Yang, Ph.D., P. E.

Department of Civil and Environmental Engineering
North Dakota State University
Fargo, North Dakota

March 2015

Acknowledgments

The Principal Investigator gratefully acknowledges all individuals who contributed to the present research report, including Dr. Saeed Ahmari, Mr. Michael Telste, Dr. Frank Yazdani, and Dr. Jimmy Kim.

ABSTRACT

This report presents a research examining the feasibility of creating an integrated structural health monitoring and impact/collision detection system for bridges in remote cold regions, where in-person inspection becomes formidable. The research report includes a theoretical analysis of the impact event identification in Chapter II, laboratory experiment verification in Chapter III, and a field testing and an integrated Structural health monitoring system in Chapter IV. Based on the systematical research outcomes, the impact/collision event and the real-time bridge structural health status have been successfully identified and recorded, which could be used for bridge management and resources allocation in future.

TABLE OF CONTENTS

LIST OF FIGURES

LIST OF TABLES

EXECUTIVE SUMMARY

This report presents a three-part research program examining the feasibility of building an integrated structural health monitoring and impact/collision detection system in remote cold regions, where in-person inspection becomes formidable. For the first phase, an algorithm is developed to identify the impact location and the impact magnitude using particle swarm optimization (PSO). The algorithm was tested using numerical models and proven to be effective in finding the impact location, the impact force magnitude, and the impact pulse frequencies. In the second phase, the developed algorithm was tested in the laboratory of North Dakota State University (NDSU). A plate with instrumented sensors is tested using impact hammers and the strain measurement with noise is considered. The developed algorithm is adopted successfully to locate the impact location, the impact magnitude, and the impact frequencies. Finally, implementation of the impact/collision system is combined with an innovative displacement based damage detection algorithm and used in a concrete bridge in Fargo, ND. The bridge was fully instrumented by BDI, Inc., and the data were collected for a static load testing. Based on the measured data, a numerical model in ABAQUS was built using the so-call grillage method and validated through the field measurements. Based on the validated model, the deformation based damage detection method is suggested. The damaged bridge responses are simulated through artificial damages (stiffness reduction) in the numerical model. From the simulated responses, the deformation based damage detection method is tested and shown finding the damage location successfully and effectively. Based on the same sensor deployment, the impact/collision event is also anticipated to be identified with minor adjustment of the boundary conditions suggested in Section 3.

1. PART IDESIGN OF THE INTEGRATED STRUCTURE HEALTH MONITORING AND IMPACT/COLLISION DETECT SYSTEM.

Structural health monitoring is a widely accepted concept in infrastructural management. Structural health monitoring of engineering structures, and particularly civil infrastructures, has been recently growing rapidly. Health monitoring can be performed in active mode by using ultrasonic actuators, which generate signals to interrogate the structure, or in passive mode, where the induced signals due to impact event is used to detect the damaged/impact points.[1-3] The former one is used in schedule-based maintenance but the latter one is applicable to condition-based maintenance. There is a tendency toward condition-based maintenance due to its low cost and convenience in contrast to the difficulties associated with schedule-based monitoring.[4-6] A typical structural health monitoring system will include sensors, data acquisition systems, communication systems, data storage, and a processing unit as shown in Figure 1.1.

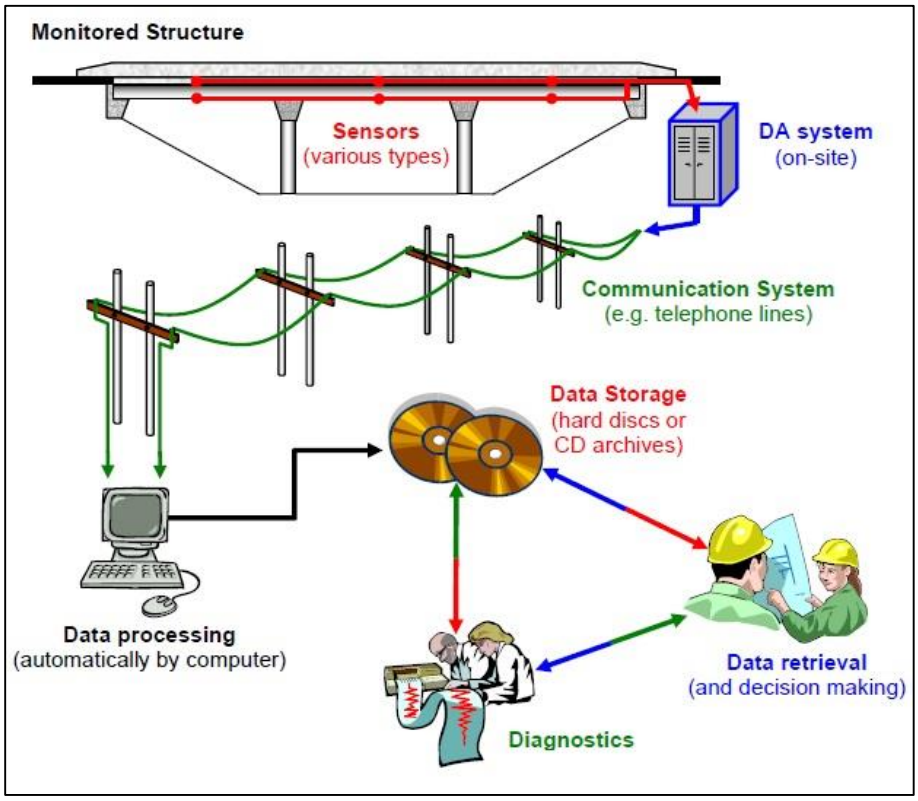

Figure 1.1 A typical structural health monitoring system

The integrated structure health monitoring and impact/collision detect system suggested in this project will be composed of sensors, a data collection system, and data processing unit. Several sensor deployments have been suggested, which have been shown in Figure 1.2.

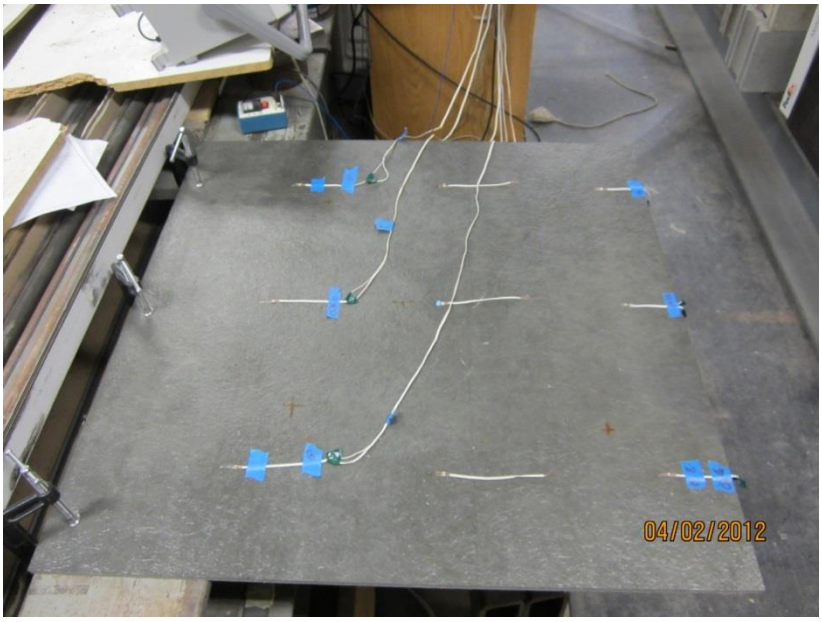

(a) Composite plate

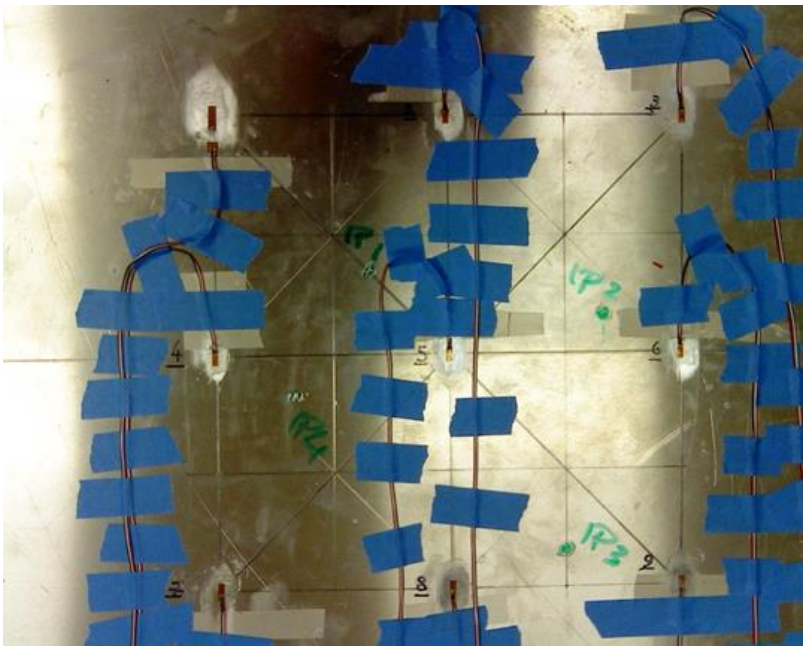
(b) Aluminum plate

(c) A Lab model 1-span steel bridge

Figure 1.2 The sensor deployment adopted in lab-pilot tests

An impact/collision detection system is also designed and shown in Figures 1.3 and 1.4. A small scale test is performed in the lab using the suggested system. The test could turn on different warning lights based on the different levels of impact inputs. When the impact level is higher over a threshold, a red light will be turned on. Otherwise, only the impact events, including impact locations and impact magnitudes, will be registered in the system. A video showing the process is included in Figure 1.5.

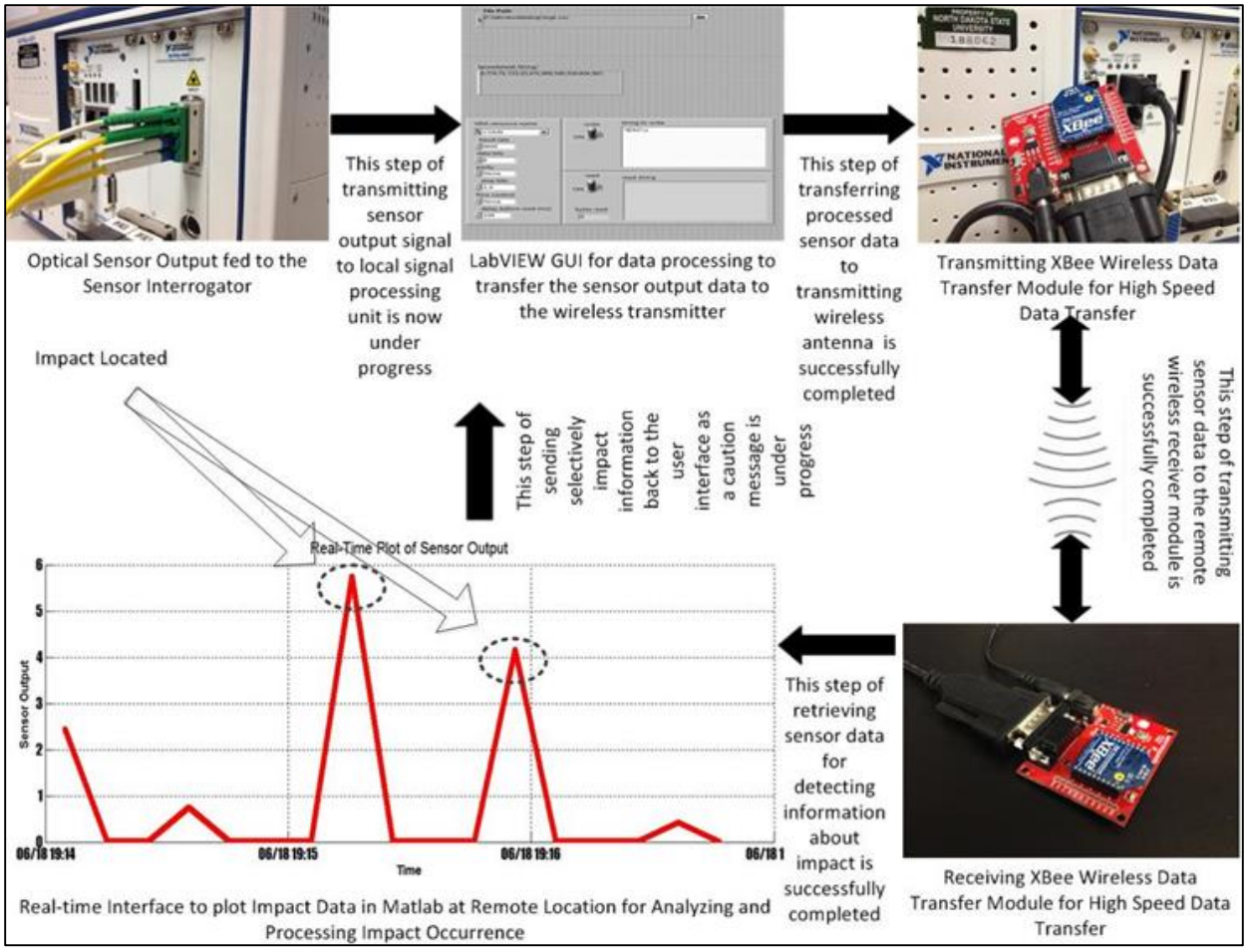

Figure 1.3 The designed impact and collision detection system

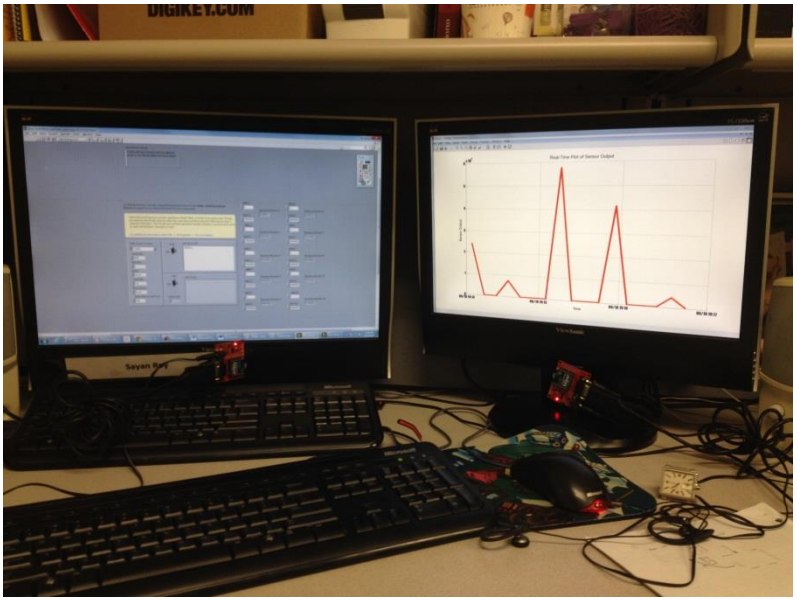

Figure 1.4 Far field control end of the impact/collision detection system

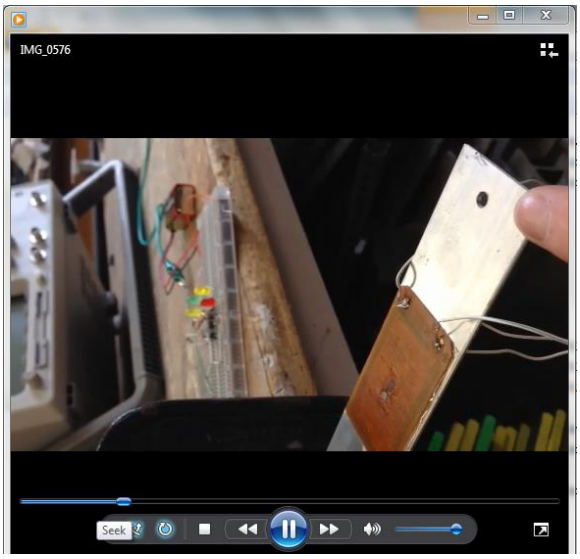

Figure 1.5 Demonstration of the warning lights for different level of impacts

2. DEVELOPMENT OF DATA PROCESSING, AND IMPACT/COLLISION EVENT EXTRACTION ALGORITHMS

2.1 Introduction

Extensive research effort in the literature has been made to identify impact load locations and impact load characteristics for different types of structures.[7-17] The IL and impact load time history (ILTH) are determined by different techniques of inverse analysis from the local sensor measurement. Inverse analysis can be performed by minimizing the error between the measured and predicted data obtained from forward solving of a mathematical model (model-based) [7-10, 12, 14, 18, 19] or by training the structure using neural network.[20-22] Model-based methods are more widely adopted by researchers. In these methods, the IL and ILTH can be simultaneously obtained by back-analysis of the mathematical model [7-9, 12] or separately using the transfer matrix method.[10, 18, 19, 23] Transfer matrix method typically needs sufficiently fine mesh since too coarse mesh leads to inaccurate results.[16] Furthermore, the transfer matrix method may not be efficient in large structures.[19]

A number of researchers have developed or adopted an optimization technique to back analyze a model-based structure. Efficiency of the algorithms is an important factor for real-time detections. In order to back-calculate the impact parameters, the objective function can be minimized with two different classes of methods: gradient-based methods and non-gradient-based methods. The main disadvantage of gradient-method is the costly computations related to the gradient and hessian matrices of complex functions [24] and only suitable start points converge to the minimum.[7] In addition, finding the global minimum is a great challenge because usually the objective functions are not uni-modal and a local minimum may be found instead. In the second type of minimization technique, heuristic global optimization techniques such as genetic algorithm (GA) and PSO are used to evaluate the objective function at certain locations until the global minimum is found.[7, 25] PSO is a heuristic algorithm that offers advantages such as simplicity and convenience in implementation, [26] and convergence for different mechanical problems can be ensured by tuning the input parameters.[25] It is a bio-inspired method in which sample points, so called "particles," are selected to cover the sampling space (dimension of space depends on the number of unknown parameters). The particles move in the sampling space and communicate with each other to find the global minimum. The process of optimization is faster as the objective function is only evaluated at certain points and a global minimum is easier to achieve by using a sufficiently broad sampling space.[27] To the knowledge of authors, PSO has not been applied to IL and ILTH identification in plate structures although it has been used in other fields.[27, 28]

The process of noisy measured responses is another problem in inverse analysis. Inverse (deconvolution) problem is an ill-posed problem. Noisy measurements lead to instable results, and objective function does not converge to zero at the minimum point.[28] Regularization of the measured data is commonly used to overcome the ill-posedness.[14, 18, 29, 30] In this case, additional condition is imposed to optimization of the objective function, which implicitly leads to filtering the noisy measured data. Tikhonov, truncation, and Singular Value Decomposition (SVD) are the common methods used by others.[14, 31] These methods are applicable to linear structural systems.[32] Nonlinearity of structure was addressed by Ma and Ho through extended Karman filter and recursive least square estimator.[33] In general, the major disadvantage with classical regularization methods is that they need to determine appropriate regularization parameters.[29]

A second approach to address the noisiness of the measured data is stochastic analysis. Stochastic analysis, unlike the deterministic methods, addresses the uncertainties associated with the structural properties such as elastic modulus and measurement error.[34] Since the goal of inverse analysis is to determine the proximity of the impact location and the impact load magnitude, stochastic analysis can be performed to find an area instead of a single impact location. Han and Kinoshta suggested a stochastic

inverse analysis for a single degree freedom (SDOF) structure to reconstruct impact load.[32] The major drawback with this method is that statistical distribution of data needs to be known. Interval analysis is an alternative to this method, in which the maximum and minimum (boundaries) of the system response are only considered.[34, 35] The output of the inverse analysis is maximum and minimum limits for the back-calculated parameters and does not give any information about the distribution of IL and ILTH. In the interval analysis method, instead of considering a deterministic value for the objective function, a range of values is obtained based on the intervals assumed for the input parameters. Essentially, it is assumed that the input consists of bounded uncertain data. The mean and radius of the interval corresponding to the objective function is then minimized.[35] Qiu and Wang used interval analysis method versus probabilistic method to find the dynamic response of a structure and concluded that probabilistic analysis leads to a tighter interval since interval analysis only considers the extreme condition.[36] Jiang et al. used interval-based inverse analysis for truss and frame [35]. They used two objective functions for minimization as the center and radius of interval need to be determined. Liu et al. combined regularization and interval analysis to reconstruct ILTH for a cylindrical shell structure under impact load at a known location.[34] Interval analysis combined with regularization method or alone based on multi-objective function (as in [35]) still might be computationally costly, especially for real-time detections.

In this project, IL and ILTH for a simply supported plate are simultaneously obtained and the uncertainty is addressed by a non-stochastic inverse analysis. The ILTH is simplified with a sinusoidal function and the dynamics of plate is described by the Whitney and Pagano's solution.[37] PSO as an efficient search method is then adopted to minimize the objective function and a new simplified method is finally developed to find the extreme limits of the IL and ILTH based on the least square method.

2.2 Identification scheme

In this study, a simple and effective scheme is proposed to identify IL and ILTH through a three-layer identification process. The three layers are integrated to effectively identify IL and ILTH in an intelligent structure, which contains a network of sensors. At least three sensors are used in this study. Initially, strain time histories that are recorded by all the sensors are evaluated and the three least time of arrivals (TOAs) corresponding to the closest sensors to the IL are selected. The IL is then estimated by the triangulation method.[8, 11, 15] In this method, IL is determined by minimization of the error between the predicted and measured TOAs. The main drawback with this method is the way to find TOAs in a noisy response. Furthermore, wave speed is not easy to find in an anisotropic plate as it depends on the propagation direction and the wave frequency. This method is modified in this study to estimate IL.[8]

The second layer of the identification process consists of detection of IL and reconstruction of ILTH by minimizing the measured and predicted strain time histories. The results of the first layer help in refining the sampling space. The noisy measured data at the location of the three sensors found in the first layer are then filtered by the moving average method and then used to determine the IL and ILTH. The third layer of identification determines the extreme ILs and ILTHs based on the maximum observed error in the measured data. The error is calculated by subtracting the filtered strain time history from the noisy one.

2.3 Theories

Layer 1: Location Estimation

Initially, TOAs need to be determined. In order to reduce the effect of noise in this stage, differential TOA is used:[11]

$$\Delta t_i = t_i - t_1 \tag{2.1}$$

where t_1 and t_i are, respectively, the TOA at the *i*-th sensor and *1*-th sensor location. Because three sensors are used in this study, *i* can take 2 and 3. The objective function is then defined as following:

$$\begin{aligned} Err &= \sqrt{(\Delta t_{2m} - \Delta t_{2c})^2 + (\Delta t_{3m} - \Delta t_{3c})^2} \\ &= \{[\Delta t_{2m} - \frac{1}{V}(\sqrt{(x_2 - \xi)^2 + (y_2 - \eta)^2} - \sqrt{(x_1 - \xi)^2 + (y_1 - \eta)^2})]^2 \\ &+ [\Delta t_{3m} - \frac{1}{V}(\sqrt{(x_3 - \xi)^2 + (y_3 - \eta)^2} - \sqrt{(x_1 - \xi)^2 + (y_1 - \eta)^2})]^2\}^{\frac{1}{2}} \end{aligned} \tag{2.2}$$

where Δt_{im}, Δt_{ic}, x_i and y_i, ξ, η, and V are, respectively, the measured differential TOA, the predicted differential TOA, *x* and *y* coordinates of the *i*-th sensor, *x* and *y* coordinates of the IL, and wave speed. In this equation, it is assumed that the plate is isotropic; otherwise, a direction-dependent wave speed needs to be used. Bending wave's speed in a plate structure can be computed from the following equation:

$$V = \sqrt[4]{\frac{Eh^2\omega^2}{12(1-\upsilon^2)\rho}} \tag{2.3}$$

where E, ν, h, ρ, and ω are, respectively, the elastic modulus, Poisson's ratio, plate thickness, unit weight, and wave frequency. Wave frequency can be computed by Fast Fourier Transform (FFT) of the sensor measurements.[8] Having wave speed and TOAs at the sensor locations, the objective function (Eq. (2.2)) can be minimized by the steepest descent method. The golden search method is adopted for linear search in the steep descent method.

Layer 2: Deterministic Identification of Impact Location and Load Characteristics

Layer 2 consists of a plate dynamics model for forward solving in order to predict the strain time history. In general, there are two classical approaches to the plate problem: Kirchhoff-Love's and Mindlin's solution. Kirchhoff-Love's formulation only takes in-plane shear into account while Mindlin's solution takes out-of-plane shear into account as well. Whitney and Pagano's solution is similar to Mindlin's solution for thick plate but it also accounts for the effects of anisotropy. Whitney and Pagano's approach [37] to plate vibrations has been adopted in this study for simply supported rectangular plate. Carvalho and Soares [38] and Dobyns [39] adopted the governing differential equations and presented a closed form solution for vertical displacements of simply supported composite plates. The same methodology can be used to derive an expression for strain along *x*-direction using the relationship between time dependent function of bending deflection and modal amplitudes [38] and following equation:

$$\varepsilon_x = z\frac{\partial \psi_x(x,y,t)}{\partial x} \tag{2.4}$$

where *z* and ψ_x are, respectively, *z*-coordinate with respect to mid-plane and bending curvature about *x*-axis. Strain along *x*-axis can be derived as follows:[38]

$$\varepsilon_x = K_c \sum_i \sum_j K_{ij} \sin(\frac{i\pi\xi}{a})\sin(\frac{j\pi\eta}{b})\sin(\frac{i\pi x}{a})\sin(\frac{j\pi y}{b})\int_0^t F(\tau)\sin[\omega_{ij}(t-\tau)]d\tau \tag{2.5}$$

Where *i, j* are mode numbers; *a* and *b*, ξ and η, and ω_{ij} are, respectively, length and width of plate, *x* and *y*-coordinate of IL, and modal frequency of the plate which can be found in [38]. K_c and K_{ij} are,

$$K_c = -\frac{8}{a\rho\pi uv} \tag{2.6}$$

$$K_{ij} = \frac{K_A}{j\omega_{ij}} sin(\frac{i\pi u}{2a}) sin(\frac{j\pi v}{2b}) \tag{2.7}$$

where *u* and *v* and K_A are, respectively, length and width of impact area and K_A is a factor depending on extensional, bending, and transverse shear stiffness of the plate.[38] In this study, very small values are chosen for *u* and *v* in order to consider pointwise impact load, however, they can be assumed to be unknown quantities such as IL and ILTH in case of impacted area. $F(\tau)$, the impact load time history, can be simplified by a half-cycle sinusoidal function,

$$\begin{aligned} &F(\tau) = 0 && for\ \tau < t_0 \\ &F(\tau) = F_0\, sin(\omega_L[\tau - t_0]) && for\ t_0 < \tau < t_1 \\ &F(\tau) = F_0\, sin(\omega_U[\tau - t_3]) && for\ t_1 \le \tau < t_2 \\ &F(\tau) = 0 && for\ t_2 \le \tau \end{aligned} \tag{2.8}$$

where F_0, ω_L, ω_U, t_0, t_1, t_2 are, respectively, impact load amplitude, loading frequency, unloading frequency, impact start time, the time corresponding to impact amplitude, and impact end time. t_0 is zero if the measurement starts at the same time that impact occurs. But, in practice, start times of impact and strain measurement are different, i.e., strain recording starts long before impact occurs. Therefore, time can be set to zero when the first signal is detected in the closest sensor, which means that the time lag between the defined start time and impact start time equals to TOA of the closest sensor. t_1, t_2, and t_3 are,

$$\begin{aligned} t_1 &= t_0 + \frac{1}{4\omega_L} \\ t_2 &= t_0 + \frac{1}{4\omega_L} + \frac{1}{4\omega_U} \\ t_3 &= t_2 - \frac{1}{2\omega_U} \end{aligned} \tag{2.9}$$

Yan and Zou simplified the ILTH with a half-cycle sinusoidal function. Their analysis results indicated that IL can be approximately detected and impact load energy and amplitude can be accurately determined despite the simplification in ILTH by sinusoidal functions. For damage detection purposes, impact load amplitude and energy are important.[7]

To facilitate the computations, the integral in Eq. (2.5) can be calculated analytically by substituting Eq. (2.8) into the integral which leads to:

$$\begin{aligned} \int F(\tau) sin[\omega_{ij}(t-\tau)]\, d\tau = {} & cos(\omega t_0) sin(\omega_{ij} t) Z_1(\tau) - cos(\omega t_0) cos(\omega_{ij} t) Z_2(\tau) \\ & - sin(\omega t_0) sin(\omega_{ij} t) Z_3(\tau) + sin(\omega t_0) cos(\omega_{ij} t) Z_4(\tau) \end{aligned} \tag{2.10}$$

where

$$Z_1(\tau) = -\frac{cos[(\omega-\omega_{ij})\tau]}{2(\omega-\omega_{ij})} - \frac{cos[(\omega+\omega_{ij})\tau]}{2(\omega+\omega_{ij})} \tag{2.11}$$

$$Z_2(\tau) = \frac{sin[(\omega-\omega_{ij})\tau]}{2(\omega-\omega_{ij})} - \frac{sin[(\omega+\omega_{ij})\tau]}{2(\omega+\omega_{ij})} \tag{2.12}$$

$$Z_3(\tau) = \frac{sin[(\omega-\omega_{ij})\tau]}{2(\omega-\omega_{ij})} + \frac{sin[(\omega+\omega_{ij})\tau]}{2(\omega+\omega_{ij})} \tag{2.13}$$

$$Z_4(\tau) = \frac{cos[(\omega-\omega_{ij})\tau]}{2(\omega-\omega_{ij})} - \frac{cos[(\omega+\omega_{ij})\tau]}{2(\omega+\omega_{ij})} \tag{2.14}$$

Having the forward solving model, the objective function is now defined as below,

$$Err = \sqrt{\sum_{i=1}^{3}\sum_{j=1}^{N}[\varepsilon_{ic}(t_j) - \varepsilon_{im}(t_j)]^2} \tag{2.15}$$

where $\varepsilon_{ic}(t_j)$ and $\varepsilon_{im}(t_j)$ are, respectively, the predicted and measured strains at the *i*-th sensor location and time t_j and N is the number of time steps. The objective function is a 6-dimensional space in terms of *X*. The variables can be written as,

$$X=X(\xi,\ \eta,\ F_0, t_0,\ \omega_L,\ \omega_U) \tag{2.16}$$

Initial sample vectors (particles) are defined in a way to cover a certain range of the six parameters. The output from Layer 1 is used to narrow the range of ξ and η. The objective function is iteratively computed for the updated vectors until all the sample vectors converge to the destination vector. At each iteration, the particle's speed and position are updated as following,

$$\vec{V}_{k+1} = \vec{A}\otimes\vec{V_k} + \vec{B_1}\otimes r_1 \otimes(\vec{P_1} - \vec{X}_k) + \vec{B_2}\otimes r_2 \otimes(\vec{P_2} - \vec{X}_k) \tag{2.17}$$

$$\vec{X}_{k+1} = \vec{C}\otimes\vec{X}_k + \vec{D}\otimes\vec{V}_{k+1} \tag{2.18}$$

where X_k and X_{k+1}, V_k and V_{k+1}, P_1, P_2, and *A* are, respectively, the particle's position (in 6 dimensions) at the *k*-th and (*k+1*)-th iteration, particle's speed at the *k*-th and (*k+1*)-th iteration, particle's past best position based on its own experience, best position experienced by other particles in the flock, and momentum factor. B_1 and B_2 are factors related to the personal influence and social influence of particles and the corresponding terms (second and third term of Eq. (2.17)) can be weighted by stochastic variables r_1 and r_2. *C* and *D*, the weight factors for updating particle's position based on its current position and speed, which can be taken as 1.[25] $\otimes$ denotes the element by element multiplication of the two matrices. If the factors are constant for all elements of the position and speed vector (*X* and *V*), *A*, B_1, and B_2 can be changed into scalars. In Eq. (2.17), the first term indicates the momentum of motion of the particles in the search space, the second term indicates the speed of the particles based on their personal experience, and the third term updates based on the social behavior of the particles and their influence on each other. Depending on the values of *A*, B_1, and B_2, long-term trend of the particles can show convergent (to the optimal position), harmonic oscillatory, and zigzagging behavior.[25] The discussed parameters can be empirically tuned to make the algorithm work efficiently.

Layer 3: Uncertain Identification of Impact Location and Load Characteristics

In case of noisy response, the measured strain time histories are first filtered and then IL and ILTH are identified through Layer 2. The back-calculated parameters are assumed to be the mean results based on the filtered measurements. The deviation of the variables $(\xi, \eta, F_0, t_0, \omega_L, \omega_U)$ from their mean values is then found by another optimization procedure in Layer 3. It is assumed that the measured data are bounded uncertain and the boundaries are deterministic values based on the observation. Strain can vary between the extreme ends and since only the deterministic boundaries are used in the analysis, the probabilistic distribution of the uncertain data is not important for the interval analysis assuming 100% level of confidence for the observed extreme errors.

Assume that strain in Eq. (2.5) is rewritten as a function of the vector $X(\xi, \eta, F_0, t_0, \omega_L, \omega_U)$,

$$\varepsilon = \varepsilon(\vec{X}) = \varepsilon(\xi, \eta, F_0, t_0, \omega_L, \omega_U) \tag{2.19}$$

Using Taylor's expansion series, the error in strain measurement can be approximated by the following equation. The linear term of Taylor series is used in this study assuming that the level of error is small.

$$\Delta\varepsilon = \frac{\partial\varepsilon}{\partial\xi}\Delta\xi + \frac{\partial\varepsilon}{\partial\eta}\Delta\eta + \frac{\partial\varepsilon}{\partial F_0}\Delta F_0 + \frac{\partial\varepsilon}{\partial t_0}\Delta t_0 + \frac{\partial\varepsilon}{\partial\omega_L}\Delta\omega_L + \frac{\partial\varepsilon}{\partial\omega_U}\Delta\omega_U \tag{2.20}$$

For simplicity in notations, IL and ILTH parameters are denoted by x_i and Eq. (2.20) is re-written as:

$$y_{s,t} = \sum_{i=1}^{6} a_i^{s,t} \times \delta x_i \tag{2.21}$$

where $y_{s,t}$ is the error at the s-th sensor location and at time t, $a_i^{s,t}$ is the gradient of strain (Eq. (2.5)) with respect to the i-th variable ($x_1 = \xi, x_2 = \eta, x_3 = F_0, x_4 = t_0, x_5 = \omega_L, x_6 = \omega_U$) at the s-th sensor location and time t, and δx_i is deviation of the i-th variable. In Eq. (2.21), the values of $y_{s,t}$ and $a_i^{s,t}$ are known at the mean $X(\xi, \eta, F_0, t_0, \omega_L, \omega_U)$ obtained in Layer 2. Eq. (2.21) can be written for "s" number of sensors and "T" number of time increments. The resulted equation in matrix form is:

$$\boldsymbol{Y} = \boldsymbol{G} \times \Delta\boldsymbol{X} \tag{2.22}$$

Eq. (2.22) is very over-determined and hence X can be estimated by calculating Moore Penrose pseudo-inverse of the matrix G (through singular value decomposition, SVD method):

$$\Delta\boldsymbol{X} = \boldsymbol{G}^{+} \times \boldsymbol{Y} \tag{2.23}$$

In order to archive the maximum values of δx_i, the absolute values of the elements of the matrices G^+ and Y are used in the calculations. In other words, to maximize δx_i,, $+ERROR$ is substituted for $y_{s,t}$ whenever it is multiplied by a positive element of G^+ and $-ERROR$ is substituted whenever it is multiplied by a negative element of G^+. This process will select the maximum and minimum values of strains to find the maximum δx_i. Minimum δx_i will be obtained in a reverse manner. For a symmetric band, a symmetric range will be obtained for δx_i, however, this is not true for asymmetric or biased errors.

2.4 Verification

Finite element model (FEM) is used to verify the forward solving mathematical model and the inverse model at Layer 1 and 2. The detected IL and reconstructed ILTH are compared with the actual IL and ILTH.

Verification of Forward Solving Model

The presented mathematical model is verified by a finite element model (FEM) using ABAQUS. An aluminum plate of 0.88 × 0.88 × 0.0025 m subjected to a sinusoidal impact load is simulated by quadrilateral shell element with reduced integration for small strains (S4RS). The plate is subjected to an impact load at the center of the plate with amplitude of 1000 N and loading and unloading frequencies of, respectively, 1000 and 300 Hz, which starts at time zero. Since only the first 1000 μS of vibration time is used, there would not be significant damping effect. The FEM contains 16,900 shell elements and 17,161 nodes. Vibrating duration is divided into 100 equal time intervals.

Figure 2.1 compares FEM and the mathematical model's results at impact location. There is a satisfactory match between the results obtained from both methods.

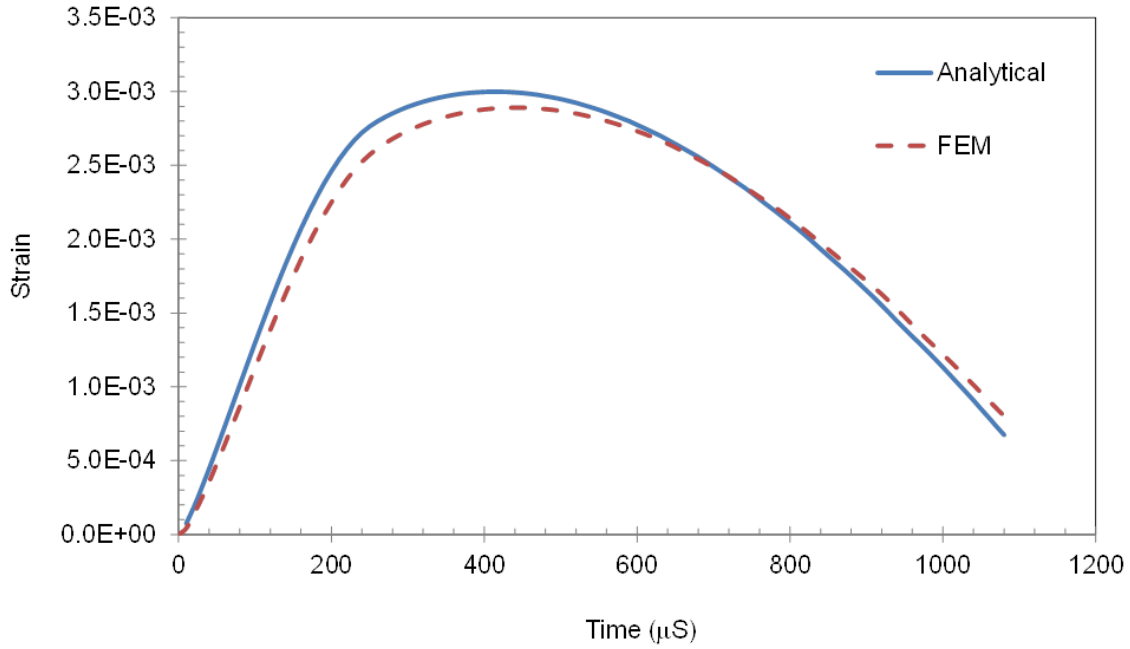

Figure 2.1 Comparison of strain time histories between the mathematical model and FEM at impact location at the center of the plate

Verification of Layer 1

The same plate with the properties shown in Table 2.1 is subjected to the same impact load for IL and ILTH identification through Layers 1 and 2. Three different points are selected as the impact location and strain time histories at 9 sensor locations are collected for IL and ILTH identification (Figure 2.2). Coordinates of impact and sensor locations are shown in Table 2.2.

In the first layer, threshold method is used to find the TOA at each sensor location. The level of threshold strain is assumed to be two times the maximum amount of noise. Time histories obtained at the three

closest sensor locations are subjected to Fast Fourier Transform (FFT) to find the dominant frequency content. Then the frequency and corresponding parameters to plate properties are substituted into Eq. (2.3) to calculate wave speed. Now, having all the required parameters, Eq. (2.2) is minimized to estimate the IL. Table 2.3 summarizes the results of IL estimation for the three impact locations. For instance, from the TOAs, it can be deducted that SENS4, SENS5, and SENS7 are the closest sensors to IL1 (Figure 2.2) and *X* and *Y*-coordinates of IL is approximated by, respectively, 20% and 9% error (origin is at the bottom left corner of the plate). In all three cases, there are relatively slight deviations from the exact impact location. This will be adjusted in the second layer of analysis.

Table 2.1 Geometrical and mechanical properties of the plate structure used in current study

Plate length	0.88 m
Plate width	0.88 m
Plate thickness	2.5 mm
Elastic modulus	69 GPa
Poisson's ratio	0.34
Unit weight	2,700 Kg/m^3
Stiffness properties	$D_{11} = D_{22} = 101.59$ Pa $D_{12} = 34.54$ Pa $D_{66} = 33.52$ Pa $A_{22} = 195$ MPa $A_{44} = A_{55} = 64.4$ MPa
Plate length	0.88 m
Plate width	0.88 m
Plate thickness	2.5 mm
Elastic modulus	69 GPa
Poisson's ratio	0.34
Unit weight	2,700 Kg/m^3
Stiffness properties	$D_{11} = D_{22} = 101.59$ Pa $D_{12} = 34.54$ Pa $D_{66} = 33.52$ Pa $A_{22} = 195$ MPa $A_{44} = A_{55} = 64.4$ MPa

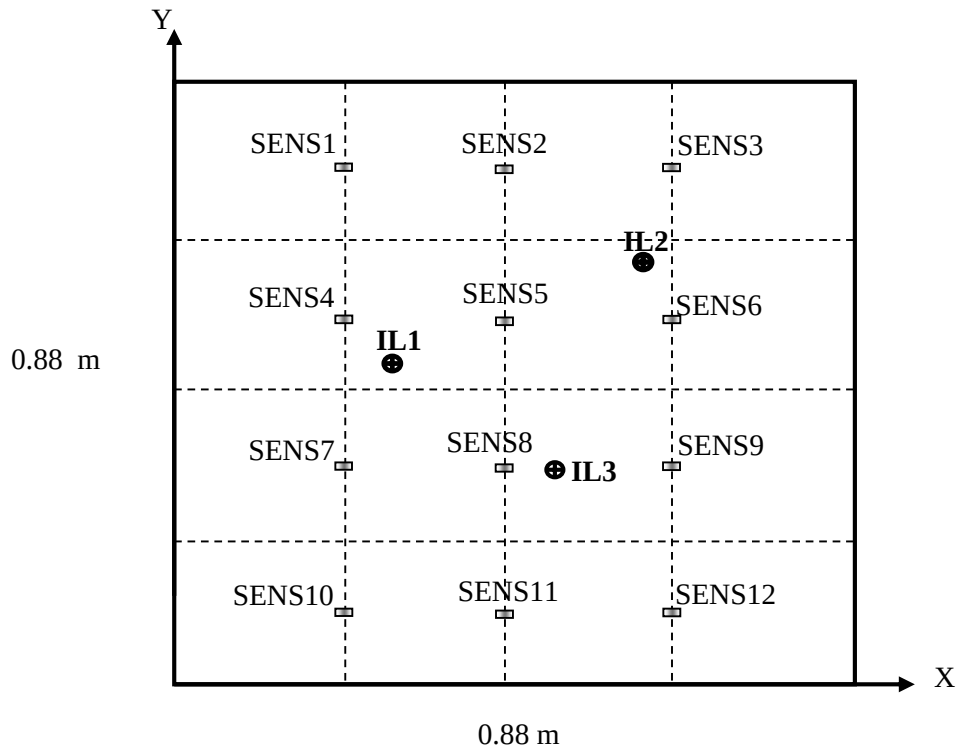

Figure 2.2 Sensors configuration and impact locations considered for the impact load (IL) and impact load time history (ILTH) identification (⊕ denotes impact location and ▭ sensor location, see Table 2.3 for coordinates).

Table 2.2 X and Y- coordinate of the IL and sensor locations in Figure 2.2

Point	X (m)	Y (m)
IL1	0.25	0.50
IL2	0.64	0.62
IL3	0.53	0.30
SENS1	0.22	0.77
SENS2	0.44	0.77
SENS3	0.66	0.77
SENS4	0.22	0.55
SENS5	0.44	0.55
SENS6	0.66	0.55
SENS7	0.22	0.33
SENS8	0.44	0.33
SENS9	0.66	0.33
SENS10	0.22	0.11
SENS11	0.44	0.11
SENS12	0.66	0.11

Table 2.3 Summary of the IL detection results from Layer 1

Time of Arrivals (μS)												
Sensor	Impact Location			Sensor	Impact Location			Sensor	Impact Location			
	IL1	IL2	IL3		IL1	IL2	IL3		IL1	IL2	IL3	
SENS1	340	480	590	SENS2	400	310	510	SENS3	530	290	490	
SENS4	130	480	400	SENS5	250	290	310	SENS6	420	300	340	
SENS7	250	570	340	SENS8	330	440	130	SENS9	480	590	250	
SENS10	600	670	410	SENS11	450	600	410	SENS12	580	540	290	
Dominant wave frequency												
Impact location			IL1			IL2			IL3			
Dominant frequency* (kHz)			2.6			3.9			4.16			
Estimated impact Location												
Impact location coordinates	IL1			IL2			IL3					
	Estimated		Target	Estimated		Target	Estimated		Target			
ξ (m)	0.31		0.25	0.56		0.64	0.52		0.53			
η (m)	0.46		0.50	0.65		0.62	0.25		0.30			

*The average of the frequencies at the three sensor locations due to impact at the indicated point is reported.

Verification of Layer 2

IL is refined and ILTH is computed in this layer. The obtained *X* and *Y*-coordinates of impact locations in the previous layer of analysis are used to define a sampling space. This helps maintain a minimum number of particles as computation costs increase with a higher number of particles due to increased number of evaluations of the objective function. The boundary formed by the surrounding sensors also helps in refining the sampling space. For example, the TOAs in Table 2.3 indicate that IL1 is contained within a square formed by SENS4, SENS5, SENS 7, and SENS 8. Now, having estimated $\xi = 0.31$ m, the closest vertical gridline has X = 0.22 m. Therefore, $\xi = 0.22$ is used as the lower bound of the sampling space. The sampling space is chosen in a way that the X and Y coordinates from layer 1 are mean of the space. It means that the upper bound for ξ is 0.40. Therefore, $\xi = 0.31$ is the mean of $\xi = 0.22 - 0.40$. In a similar way, $\eta = 0.37$ and 0.55 is used as the sampling space for η.

Results of parameter tuning of *A*, B_1, and B_2 matrices are as follows:

$$A = \begin{bmatrix} 0.7 \\ 0.7 \\ 0.2 \\ 0.9 \\ 0.1 \\ 0.2 \end{bmatrix} \quad B_1 = B_2 = \begin{bmatrix} 0.5 \\ 0.5 \\ 0.1 \\ 0.5 \\ 0.1 \\ 0.1 \end{bmatrix} \tag{2.24}$$

Figure 2.3 shows fitness convergence of the three analyses corresponding to the three impact locations. Fitness is calculated by summing the inverse of the values of objective function for each particle at each iteration. The analyses for IL1 and IL3 converge at 70 iterations and for IL2 at about 80 iterations.

However, the ultimate fitness values are different, indicating different levels of accuracy for different impact locations. The identified ILs for IL1, IL2, and IL3 and the corresponding reconstructed load time histories are, respectively, shown in Figure 2.4. An estimated location with an error of 1.9% – 24% is obtained through the triangulation method (Table 2.3) and it is adjusted in the second layer of analysis with an error ranging between 0.02% and 2.7%. ILTH match quite well with the actual time history, showing an error of about 5.3% for amplitude, 1.7% and 3.1%, respectively, for loading and unloading frequencies, and 3.4% for t_0 at the IL2 impact location.

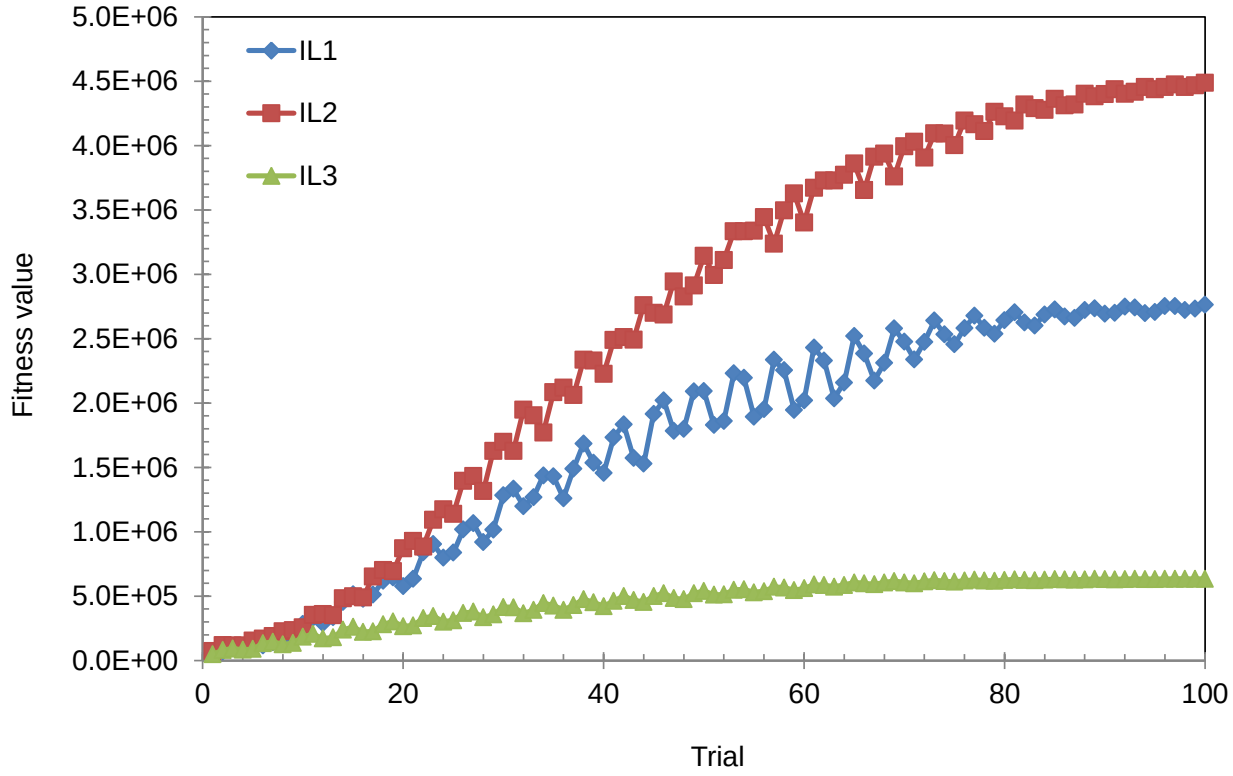

Figure 2.3 Fitness value vs. number of iterations for particle swarm optimization (PSO) of the three impact locations (see Figure 2.2 for impact locations)

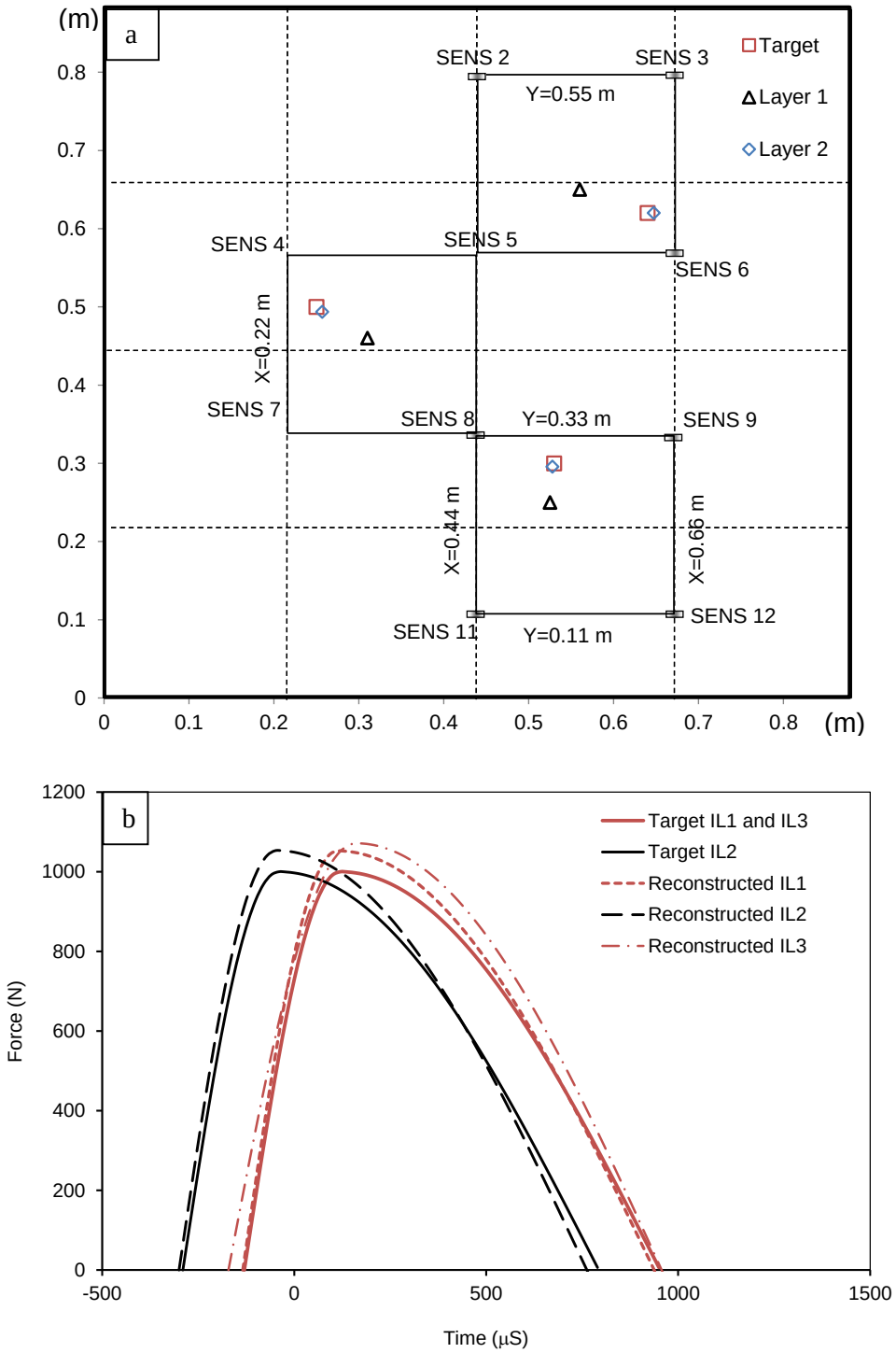

Figure 2.4 a) Deterministic impact load identification results obtained from triangulation (Layer 1) and particle swarm optimization (PSO) methods (Layer 2), b) Comparison of the target and reconstructed impact load time history (ILTH) at different ILs

2.5 Identification of impact location and load characteristics from noisy response

In the previous inverse analyses, deterministic time histories obtained from the FE model were used to identify IL and ILTH. However, in practice, the strain measurements are noisy and thus cause numerical instability. Therefore, the obtained strain time histories at all sensor locations due to impact load at IL2 location are used to synthesize a noisy response. The noisy response is synthesized by the following equation:[34]

$$\varepsilon_{noisy} = \varepsilon_{FEM} + NSL \times STD \times RND(-1,+1) \tag{2.25}$$

where ε_{noisy}, ε_{FEM}, *NSL*, *STD*, and *RND*(-1,+1) are respectively noisy strain time history, theoretical time history obtained from FE analysis, a factor indicating noise level, standard deviation of the theoretical strain time history, and a random number between -1 and 1. In this study, two noise levels, 5 and 10%, are used.

The synthesized noisy time histories are used to detect IL and reconstruct ILTH through the 1st to 3rd layers of the discussed identification scheme. 1st and 2nd layers calculate the mean IL and ILTH and the 3rd layer determines the possible extreme bounds of IL and ILTH due to uncertainty in the measurement. In order to process the data through the first and second layers, the noisy responses are filtered by moving average method with a period of 5 (for a total of 100 data points at each sensor location). TOAs are found from the filtered time histories and the three least ones are selected for the first layer of analysis. Approximation in the strain time history due to filtration results in error in TOAs. Introduction of error in TOA due to presence of noise in the response is also reported by others.[8, 11] TOAs corresponding to 5% and 10% noise levels are summarized in Table 2.4. The filtered data show up to 53% difference in TOAs with respect to the ones obtained from noiseless data (Table 2.4). Here, the grid lines are not used to confine the potential impact area because, in general (depending on noise level), inaccurate TOAs might be misleading in finding the closest sensors. The estimated IL coordinates for 5% and 10% noise levels are ξ = 0.59 and 0.64, η = 0.55 and 0.65, which show up to 14% error with respect to the actual ones.

Table 2.4 Summary of the IL detection results from Layer 1 for noisy time histories due to impact at IL2

Time of Arrivals (μS)								
Sensor	Noise level		Sensor	Noise level		Sensor	Noise level	
	5%	10%		5%	10%		5%	10%
SENS1	480	520	SENS2	310	310	SENS3	250	300
SENS4	440	510	SENS5	290	290	SENS6	140	300
SENS7	610	570	SENS8	430	440	SENS9	580	590
SENS10	700	700	SENS11	610	600	SENS12	580	590

Dominant wave frequency		
Noise level	5%	10%
Dominant frequency* (kHz)	3.9	3.9

Estimated impact Location			
	5% Noise level	10% Noise level	Target
ξ (m)	0.59	0.55	0.64
η (m)	0.64	0.65	0.62

In the second layer, the mean IL and ILTH are computed based on the filtered data. Then the error for each selected sensor (at Layer 1) is calculated by deducting the filtered data from the noisy data. The maximum measurement error for each sensor is substituted into Eq. (2.23). Having the measurement errors, Layer 3 of the analysis is performed to compute the ultimate deviation from the mean IL and ILTH. Figure 2.5 shows the actual IL2, estimated IL with Layer 1, adjusted IL with Layer 2, and the deviations from the mean points. It can be seen that the actual point is within the rectangle, which shows locus of likely impact points depending on the deviations in the strain measurements, and the boundaries are the likely impact points based on the maximum measurement errors. The deviation zone significantly expands with noise level from 5% to 10%.

Figure 2.6 illustrates the reconstructed ILTH based on the filtered strain time histories, the actual ILTH, and the maximum/minimum limits of ILTH obtained from the third layer of analysis for 5% noise level. The maximum and minimum impact load characteristics for 5% and 10% noise levels are summarized in Table 2.5. Due to large variation of frequencies, the upper lower bound ILTHs are plotted with the mean frequencies and start time and upper and lower amplitudes. At 5% noise level, t_0 varies from -280.1 to 0 μS covering a wide range including the actual t_0 = -140 μS. The actual t_0 is found through the deterministic numerical responses using the threshold criteria (the threshold for the 5% noise case is 8.46E-6; the threshold for the 10% noise case is 3.46E-5). According to the convention, positive t_0 has no physical meaning, therefore only negative sampling space is used in the PSO algorithm. In Figure 2.6, the upper and lower bound curves do not start at the extreme start points. In practice, as discussed earlier, the amplitude and energy of the impact load are important for health assessment, therefore, shifting the curves in time would not affect its momentum or energy.

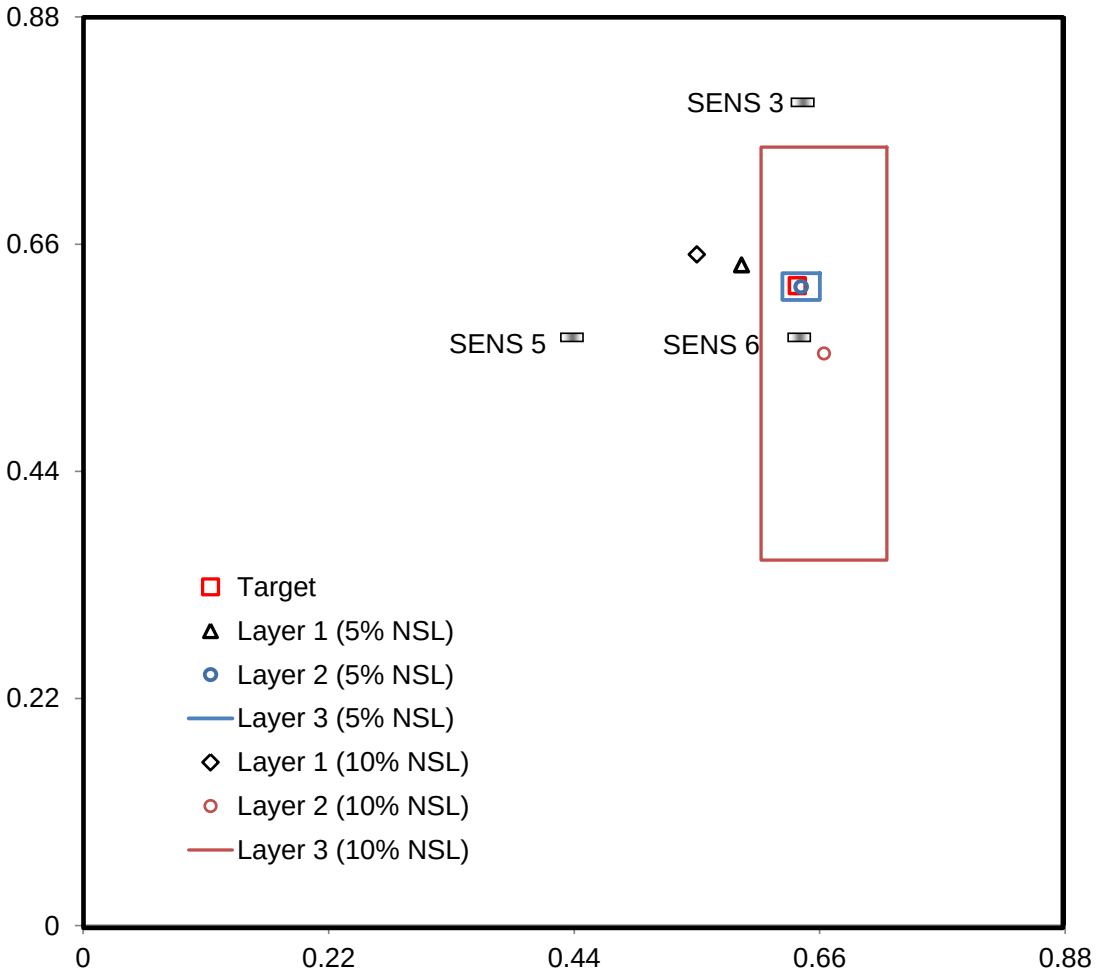

Figure 2.5 Uncertain identification of impact load location for noise levels of 5% and 10% (NSL denotes noise level)

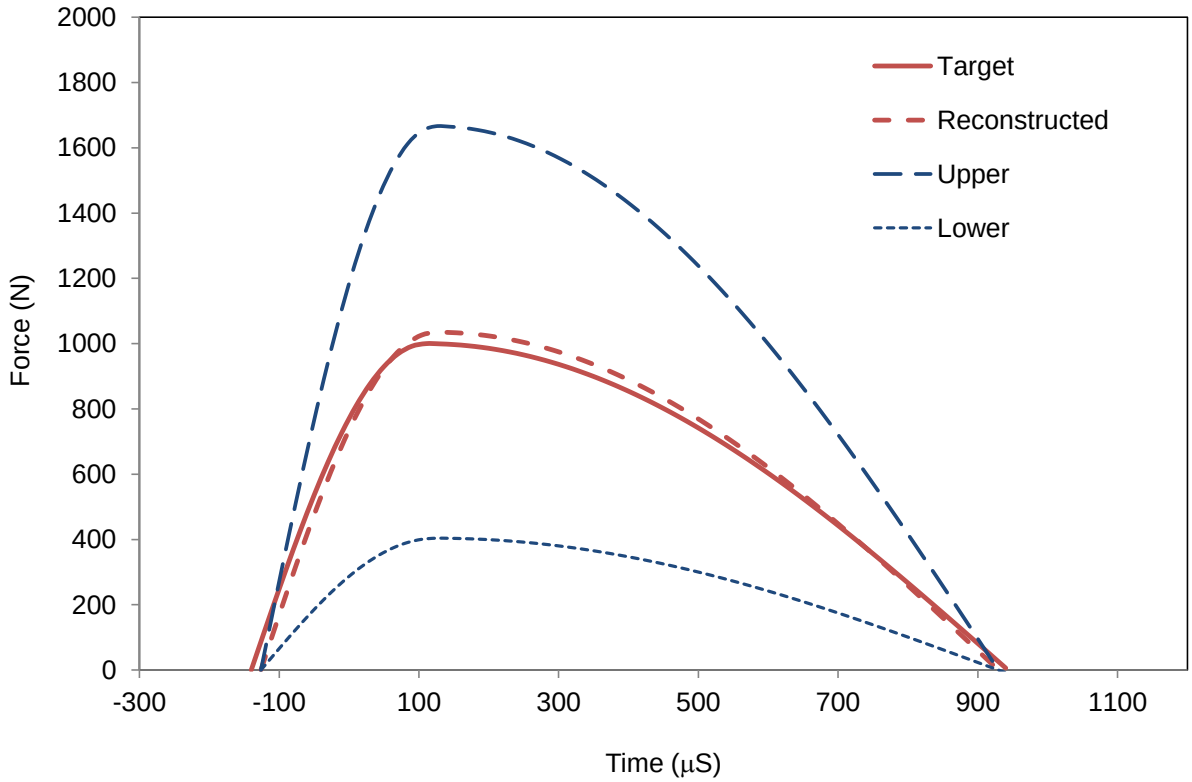

Figure 2.6 Uncertain identification of impact load time history at 5% noise level

Table 2.5 Maximum and minimum impact load characteristics (at IL2) obtained from Layer 3 assuming 5% and 10% noise level

Parameters		F_0 (N)	ω_L (Hz)	ω_U (Hz)	t_0 (μS)
Actual	5% noise	1000	1000	300	-140.0
	10% noise	1000	1000	300	-300.0
Reconstructed (mean)	5% noise	1034.9	997.2	310.6	-126.1
	10% noise	958.0	776.4	285.3	-499.4
5% noise	Maximum	1665.9	1172.2	437.6	0
	Minimum	403.9	822.2	183.6	-280.1
10% noise	Maximum	2006.5	916.69	350.4.2	0
	Minimum	0	636.1	220.2	-797

The numerical scheme presented in Eqs. (2.19) through (2.23) is based on the assumption that the variations in strain are small enough that the nonlinear terms of Taylor's series can be ignored. Otherwise, higher orders must be included in the approximation, which is beyond the scope of this study. Linear approximations are valid for the points close to the mean point or sufficiently low noise level. In practice, higher noise levels are rarely encountered and thus linear approximation can lead to sufficiently accurate results within practical ranges.

2.6 Conclusions

A numerical scheme based on inverse analysis techniques is proposed to identify impact location (IL) and impact load time history (ILTH) for a simply supported plate. The proposed model offers a computationally efficient and inexpensive method, including a heuristic algorithm for optimization and a simplified interval analysis to account for the presence of noise in the system response. Although the proposed scheme is based on a mathematical forward solving model for a simply supported plate, it can be extended to other types of structures provided a suitable mathematical model is available.

Implementation of the numerical scheme on a $0.88 \times 0.88 \times 0.0025$ m aluminum plate indicates efficiency and accuracy of the proposed model in detection of IL and ILTH. The deviations in IL and ILTH caused by the presence of noise in the system response were successfully predicted with the linear approximation principle and the least square regression. The analyses for different noise levels indicated that the actual impact location and the time history lie inside the deviation's boundaries.

3. EXPERIMENTAL VALIDATION OF THE IMPACT/COLLISION DETECT SYSTEM

Associated with the theoretical model, an impact experiment on plate structures is conducted by implementing the layered analysis with some modifications on the objective functions. Two main goals are followed with the implementation study. First, the effect of measurement noise on the inverse problem is studied, and second, suitability of different proposed options for each layer of analysis is discussed. For layers 1 and 2, different alternatives, beside the one that was already proposed, are compared and the best ones are selected for further analysis. The experiment is conducted at different locations and the contaminated measured data with noise are filtered to two different levels to study the effect of noise filtering on the final results at each layer.

3.1 Theory

Layer 1

For layer 1, IL is estimated using three options:

1. IL is estimated using the classical triangulation method. TOA is found using the threshold method. Threshold is assumed to be two times the noise level before the experiment starts.
2. This option is similar to the first option but TOA is obtained in a different way. The measured signal is filtered by taking its integral with respect to time. Then option 1 is repeated using the integral of the measured signals.
3. IL is calculated from weighted average of coordinates of the closest sensors. The weights are normalized signal energy (NSE) at each sensor location. The closest sensors exhibit the greatest NSE values.

The first two options involve triangulation method through which the error between the measured and predicted TOAs is minimized for the three closest sensors. TOA is found at all sensor locations and the three smallest ones are selected for the triangulation. Minimization procedure is performed by the steepest descent method. The golden search method is used for the linear search in the steep descent method. The cost function is:

$$\begin{aligned} Error^2 &= (\Delta t_{2m} - \Delta t_{2c})^2 + (\Delta t_{3m} - \Delta t_{3c})^2 \\ &= (\Delta t_{2m} - \frac{1}{V}[\sqrt{(x_2-\xi)^2 + (y_2-\eta)^2} - \sqrt{(x_1-\xi)^2 + (y_1-\eta)^2}])^2 \\ &+ (\Delta t_{3m} - \frac{1}{V}[\sqrt{(x_3-\xi)^2 + (y_3-\eta)^2} - \sqrt{(x_1-\xi)^2 + (y_1-\eta)^2}])^2 \end{aligned} \tag{3.1}$$

where Δt_{im}, Δt_{ic}, x_i and y_i, ξ, η, and V are, respectively, the measured differential TOA, the predicted differential TOA, x and y coordinates of the i-th sensor, x and y coordinates of the IL, and wave speed. To calculate differential TOAs, one sensor such as sensor 1 is used as the reference. Differential TOAs at other sensor locations are obtained by subtracting TOA at sensor 1 location from the other TOAs. Bending wave's speed in a plate structure can be computed from the following equation:

$$V = \sqrt[4]{\frac{Eh^2\omega^2}{12(1-\upsilon^2)\rho}} \tag{3.2}$$

where E, ν, h, ρ, and ω are, respectively, the elastic modulus, Poisson's ratio, plate thickness, plate unit weight, and wave frequency. The measured data are subjected to Fast Fourier Transform (FFT) then the dominant frequency is substituted into Eq. (2).

In the third option, first, the measured signals at the three closest sensor locations are squared and then normalized as:

$$\varepsilon_i^n(t) = \frac{\varepsilon_i^2(t)}{\sum_{j=1}^{4} \varepsilon_j^2(t)} \tag{3.3}$$

Then the normalized signal energy (NSE) is:

$$E_i^n = \int_{t_i}^{t_f} \varepsilon_i^n(t)dt \tag{3.4}$$

where t_i and t_f are arbitrary time limits for the integration (start time in this study is close to TOA but it does not have to be exactly TOA).

If the sensors are sufficiently close to the IL, it can be assumed that the NSE is linearly proportional to the distance of sensor from IL. Having signal energy at three sensor locations, the IL is estimated by:

$$\begin{aligned} \xi &= \sum_{i=1}^{n} E_i^n x_i \\ \eta &= \sum_{i=1}^{n} E_i^n y_i \end{aligned} \tag{3.5}$$

As will be shown later, NSE will be linearly dependent on time but un-normalized signal energy exhibits nonlinear relationship with time. In other words, the rate of change of energy with time (power) is constant for the normalized one, which can be used as a characteristic response of the structure. In addition, normalization of signal energy makes it less dependent or independent of impact amplitude. This will be discussed in details later.

Layer 2

In layer 2, a mathematical model for the plate structure is obtained to predict the strain at sensor locations. Then the defined cost function is minimized to fit the predicted results to the measured ones. Whitney and Pagano's approach [37] to plate dynamics has been adopted in this study for a simply supported rectangular plate:

$$\varepsilon_x = K_c \sum_i \sum_j K_{ij} \sin\left(\frac{i\pi\xi}{a}\right)\sin\left(\frac{j\pi\eta}{b}\right)\sin\left(\frac{i\pi x}{a}\right)\sin\left(\frac{j\pi y}{b}\right)\int_0^t F(\tau)\sin[\omega_{ij}(t-\tau)]d\tau \tag{3.6}$$

Where i, j are mode numbers; a and b and ω_{ij} are, respectively, length and width of plate and modal frequency of the plate.[38] K_c and K_{ij} are parameters related to geometry of the plate, dimensions of impact area, and modal frequency.[38] Particle swarm optimization (PSO) is adopted for the inverse analysis.

Since the optimization procedure becomes too slow with a high number of unknowns, the impact load is simplified with two quarter cycles of sinusoidal functions:[12, 16]

$$\begin{aligned} &F(\tau)=0 && for\ \tau<t_0\\ &F(\tau)=F_0\ sin(\omega_L[\tau-t_0]) && for\ t_0<\tau<t_1\\ &F(\tau)=F_0\ sin(\omega_U[\tau-t_3]) && for\ t_1\le\tau<t_2\\ &F(\tau)=0 && for\ t_2\le\tau \end{aligned} \tag{3.7}$$

where F_0, ω_L, ω_U, t_0, t_1, t_2 are, respectively, impact load amplitude, loading frequency, unloading frequency, impact start time, the time corresponding to impact amplitude, and impact end time. Therefore, the unknowns are coordinates of IL, loading and unloading frequencies (ω_L and ω_U), start time (t_0), and impact load amplitude (F_0). Substituting Eq. (3.7) into Eq. (3.6) yields an expression, which is linearly proportional to F_0, therefore, by normalization, signal energy becomes independent of F_0. In practice, there might be a difference between real and simplified ILTH. In this case, by normalization, degree of dependency on F_0 decreases. Normalized signal energy will be used as an alternative cost function in second layer. Having the mathematical model and simplified ILTH, three options are evaluated for layer 2:

1. OPT1: The difference between the predicted and measured strain is minimized to obtain the unknown. The objective function is:

$$Error^2=\sum_{i=1}^{3}\sum_{j=1}^{N}[\varepsilon_{ic}(t_j)-\varepsilon_{im}(t_j)]^2 \tag{3.8}$$

   where $\varepsilon_{ic}(t_j)$ and $\varepsilon_{im}(t_j)$ are, respectively, the predicted and measured strains at the i-th sensor location and time t_j and N is the number of time steps.
2. OPT2: The inverse analysis is performed in two sub-layers: 2-A and 2-B. In 2-A all the unknowns are found (ξ, μ, ω_L, ω_U, and t_0) except impact amplitude. First strain energy is normalized with respect to the closest sensors. Then the normalized strain energies are used in Eq. (3.8). This leads to an objective function independent of F_0. Having all the unknowns from sub-layer 2-A, Eq. (3.8) is again minimized with only one unknown (F_0) and using strain at sensor locations. The reason for using this option is that PSO initially needs to define particles which cover the search space. With a larger number of particles more accurate results are obtained but it makes the optimization process slower. By dividing layer 2 into two sub-layers, the number of particles is reduced, hence, optimization process becomes faster. If the range of impact amplitude is divided into 5 intervals in the previous alternative, the total number of particles will be divided by five in sub-layer 2-A.
3. OPT3: The third option is similar to the first option; however, un-normalized (average) signal power is used in Eq. (3.8). Average signal power is the signal energy divided by duration. Therefore, the objective function is:

$$Error^2=\sum_{i=1}^{4}(P_{ic}-P_{im})^2 \tag{3.9}$$

where P_{ic} and P_{im} are the predicted and measured signal power at the i-th sensor location, and the signal power is:

$$\boldsymbol{P_i}=\frac{\int_{t_i}^{t_f}\varepsilon_i^2(\boldsymbol{t})\boldsymbol{dt}}{\boldsymbol{t_f}-\boldsymbol{t_i}} \tag{3.10}$$

In this method, 4 sensors are used.

Minimization in layer 2 is performed by the PSO method. This is a heuristic method, which is inspired by the fact that a flock of birds or fish find their way in search of food while they maintain their distance from each another constantly and adjust their speed intelligently to find the shortest distance to food. In this method, a set of particles, which cover a pre-defined range of the unknown parameters (6 parameters in this study) are used as a flock of birds and their values are changed iteratively until the cost function is minimized. During each iteration, the values of the particles are changed based on their momentum, their personal experience, and their communication with others so that the updated values result in a better fitness value.

The effect of system error on inverse procedure

The two options considered for layer 2 of the inverse procedure, OPT1 and OPT3, will be later investigated in terms of the effect of the discrepancy between the forward solving model (FSM) and the experiment. Essentially, in an inverse problem, FSM iteratively predicts the signal data and then is matched with the measurements. If FSM is unable to accurately simulate the real structure due to inconsistency in boundary conditions, imperfections, or any other dissimilarities, the unknown parameters would be back calculated with a lower precision. System error is always inevitable, so the goal of this study is to find an effective cost function that is less sensitive to system errors. Error in strain at a certain location can be approximated linearly by the first terms of Taylor's series as:

$$\Delta\varepsilon = \frac{\partial\varepsilon}{\partial\xi}\Delta\xi + \frac{\partial\varepsilon}{\partial\eta}\Delta\eta + \frac{\partial\varepsilon}{\partial F_0}\Delta F_0 + \frac{\partial\varepsilon}{\partial t_0}\Delta t_0 + \frac{\partial\varepsilon}{\partial\omega_L}\Delta\omega_L + \frac{\partial\varepsilon}{\partial\omega_U}\Delta\omega_U \tag{3.11}$$

where $\Delta\varepsilon$ is the maximum system error. Eq. (3.11) is over determinate since it has 6 unknowns (deviation in the parameters) and there are as many equation as the number of sensors multiplied by the number of discretized time points. The set of equations can be solved using the least square method. In OPT3, however, average signal power is used, therefore, Eq. (3.11) is converted to:

$$\Delta\boldsymbol{P} = \frac{\partial\boldsymbol{P}}{\partial\xi}\Delta\xi + \frac{\partial\boldsymbol{P}}{\partial\eta}\Delta\eta + \frac{\partial\boldsymbol{P}}{\partial\boldsymbol{F}_0}\Delta\boldsymbol{F}_0 + \frac{\partial\boldsymbol{P}}{\partial\boldsymbol{t}_0}\Delta\boldsymbol{t}_0 + \frac{\partial\boldsymbol{P}}{\partial\omega_{\boldsymbol{L}}}\Delta\omega_{\boldsymbol{L}} + \frac{\partial\boldsymbol{P}}{\partial\omega_{\boldsymbol{U}}}\Delta\omega_{\boldsymbol{U}} \tag{3.12}$$

Derivative of P_i can be expresses as derivative strain using Eq. (3.10) as:

$$\frac{\partial\boldsymbol{P_i}}{\partial\xi} = \frac{\partial}{\partial\xi}\int_0^t \frac{\varepsilon_i^2(\boldsymbol{t})}{\boldsymbol{t}}\boldsymbol{dt} = \int_0^t \frac{2\varepsilon_i(\boldsymbol{t})}{\boldsymbol{t}}\frac{\partial\varepsilon_i(\boldsymbol{t})}{\partial\xi}\boldsymbol{dt} \tag{3.13}$$

Please note only the derivative with respect to ξ is shown here and the derivatives with respect to other variables are calculated in the same way. Hence, having derivatives of strain, derivatives of power can be readily calculated. Eq. (3.12) can be set for the three surrounding sensors, therefore, unlike Eq. (3.11), Eq. (3.12) will be determinate. By solving the system of equations and obtaining the deviation in the IL and ILTH parameters, sensitivity of the two cost functions to a certain level of system error can be compared. The maximum observed system error must be used in the equations in order to reach the maximum possible deviations in the IL and ILTH parameters.

3.2 Experimental results

The experimental setup consists of a square aluminum plate of 0.88 m width and 0.0025 m thickness (Figure 1.2). The plate is simply supported on a rigid steel frame. To create a simply supported boundary

condition, the plate is clamped between a thin circular tube at bottom and a rectangular tube on top of it. The circular tube is then welded to the top of a frame made with rectangular tubes, and the set-up is supported by columns. The columns are fixed on a floor with heavy weights to prevent rigid movement of the footings during the experiment. Figure 3.1 shows the experiment setup. A sensor grid consisting of nine sensors and four grids is created with the sensors equally spaced at approximately 0.15 m. The center of the grid network lies at the center of the plate and the distance between the outer sensors of the grid with the boundaries is maximized to minimize the effect of reflected waves at the boundaries on the strain measurements. This might give rise to system error in case the boundaries are not perfectly acting as simple supports. Since Eq. (3.6) is developed for simply supported plates, it is important to create consistent conditions or avoid this effect by making sure there's sufficient distance from the boundaries. Because, for the inverse analysis, only the initial portion of the signals will be used, boundary would not have significant effect in this experiment if sufficient distance is kept. In this experiment, the boundary-sensor distance is approximately two times the spacing between the sensors. Most of the reported experiments in the literature have used piezoelectric sensors (PZT), however, in this experiment standard strain gauges are selected due to their cost-effectiveness. The strain gauges used in this experiment are 120 Ohm provided by Micro-measurements of Vishay Precision Group. They are firmly bonded to the plate according to ASTM E1237. To enhance resolution and sensitivity, a strain gauge signal conditioner is used with a half-bridge Wheatstone. The data were recorded with two National Instrument PCI-6221 data acquisition cards. Totally, 10 channels are used, including one for the impact hammer. To ensure that the data acquisition system can handle the high frequency data reading, a maximum of five channels were used on each PCI card. Labview v. 2011 is used to record and process the data. Since practically the software is unable to record the signal data at an arbitrarily high frequency, the data are filtered at a certain cut-off frequency. Very low cut-off frequency is more convenient for handling the data but leads to inaccurate results. Therefore, the experiment is repeated at least two times at filtering cut-off frequencies of 2000 and 5000 Hz to examine this effect on each layer of the analysis. Four trials are repeated by impacting four different locations each time at a different grid. A sampling rate of 40 KHz is used with a total of 20,000 samples to cover 0.5 seconds. An impact test was conducted by a PCB hammer 086C03 model and the signal produced by the hammer was amplified by a signal conditioner.

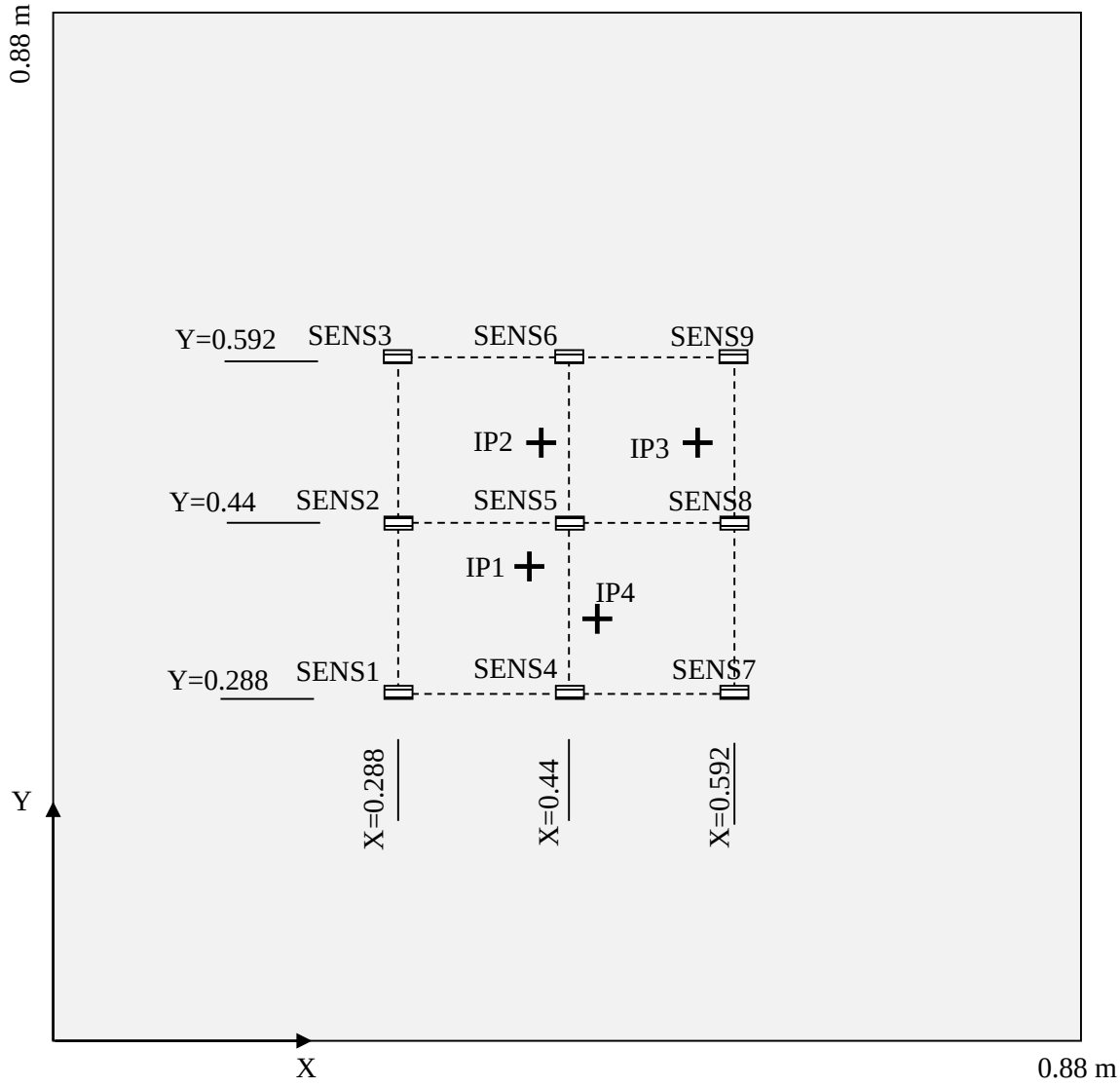

Figure 3.1 Experiment setup

3.3 Verification of the forward solving model (FSM)

The experimental results obtained at 5000 Hz cut-off frequency and at impact locations IP3 and IP4 are used to verify the plate dynamic model described above. In Figure 3.2, the comparison indicates that the FSM results match well with the experiment measurements up to a certain time, until 0.05 s after the sensor is triggered in this specific example. The main reason is that the dynamic plate model does not consider damping effect but as Figure 3.2 shows, there is a notable damping in the signals. Moreover, reflection of the impact wave from the boundaries would be the reason for the discrepancy due to imperfections in the boundaries. Although the simply supported boundary condition was provided, it is difficult to provide such an ideal boundary condition in practice. At prolonged durations, sufficient time is allowed for the reflected waves to arrive at the sensor locations and mixed with the decayed incident waves. In this study, only the initial portion of the signals are used for the inverse analysis, in which the effect of damping and boundary effects are neglected.

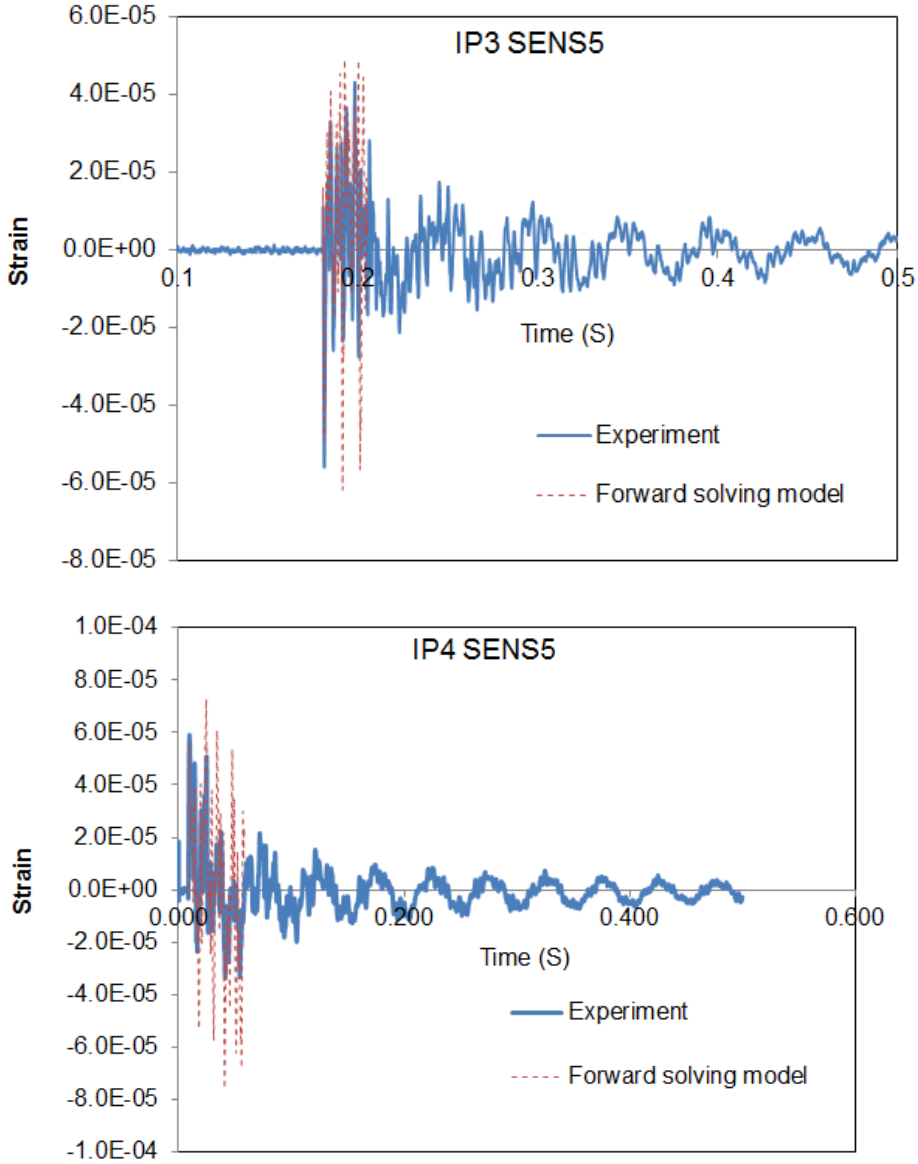

Figure 3.2 Comparison of strain time history obtained from the experiment and forward solving model at SENS5 location (see Figure 3.1) for the impact at IP3 and IP4 locations

Figure 3.3 illustrates the measured ILTH at IP4 with 5000 kHz cut-off frequency and the simplified ILTH with the sinusoidal equation [Eq. (3.7)]. It can be seen that the impact force has a sinusoidal shape followed by few peaks, which may be due to noise or multiple impact. The simplified equation fits well to the loading portion of the curve, but the unloading portion does not match quite well because the measured ILTH exhibits upward convex curvature. In order to study the importance of this discrepancy and its effect on the strain measurements, Eq. (3.6) is solved without substituting Eq. (3.7) in it, which means that the convolution integral is calculated numerically with the discrete data points of ILTH obtained from the experiment. The comparison is shown in Figure 3.4. It can be seen that discretization of the measured ILTH does not lead to a significant difference in the results with the sinusoidal load. Rather, presence of noise in the measured ILTH results in a less accurate match with the strain measurements.

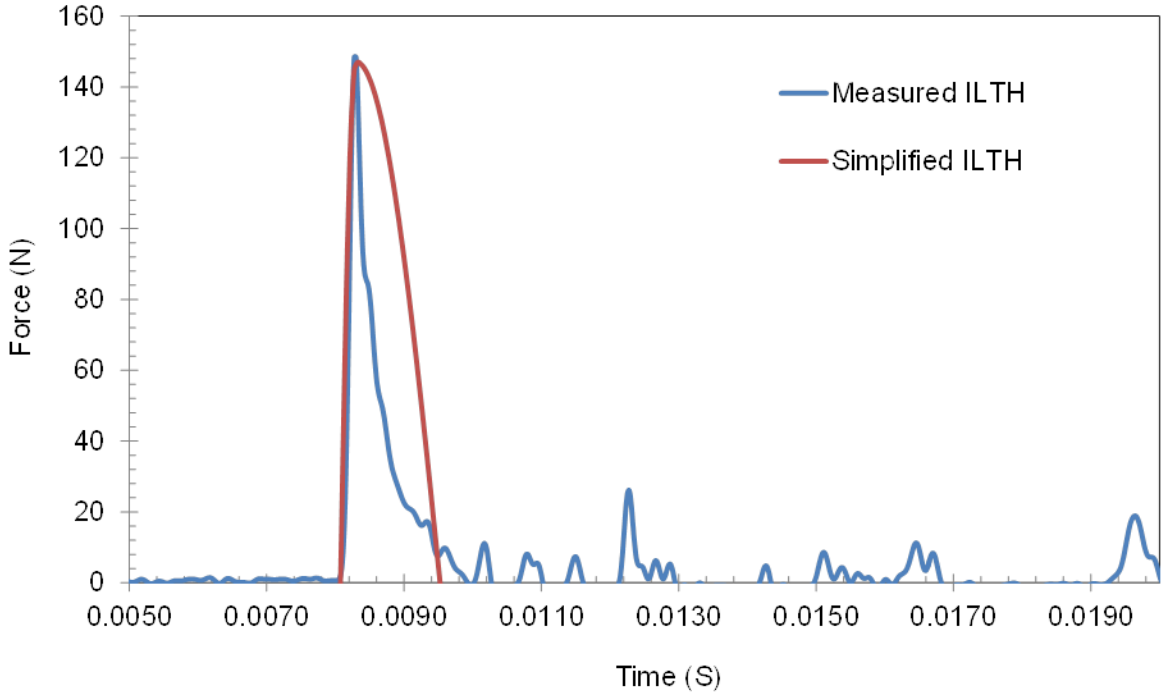

Figure 3.3 Measured impact load time history (ILTH) and its simplified pulse using Eq. (3.7) for the IP4 with 5000 kHz cut-off frequency

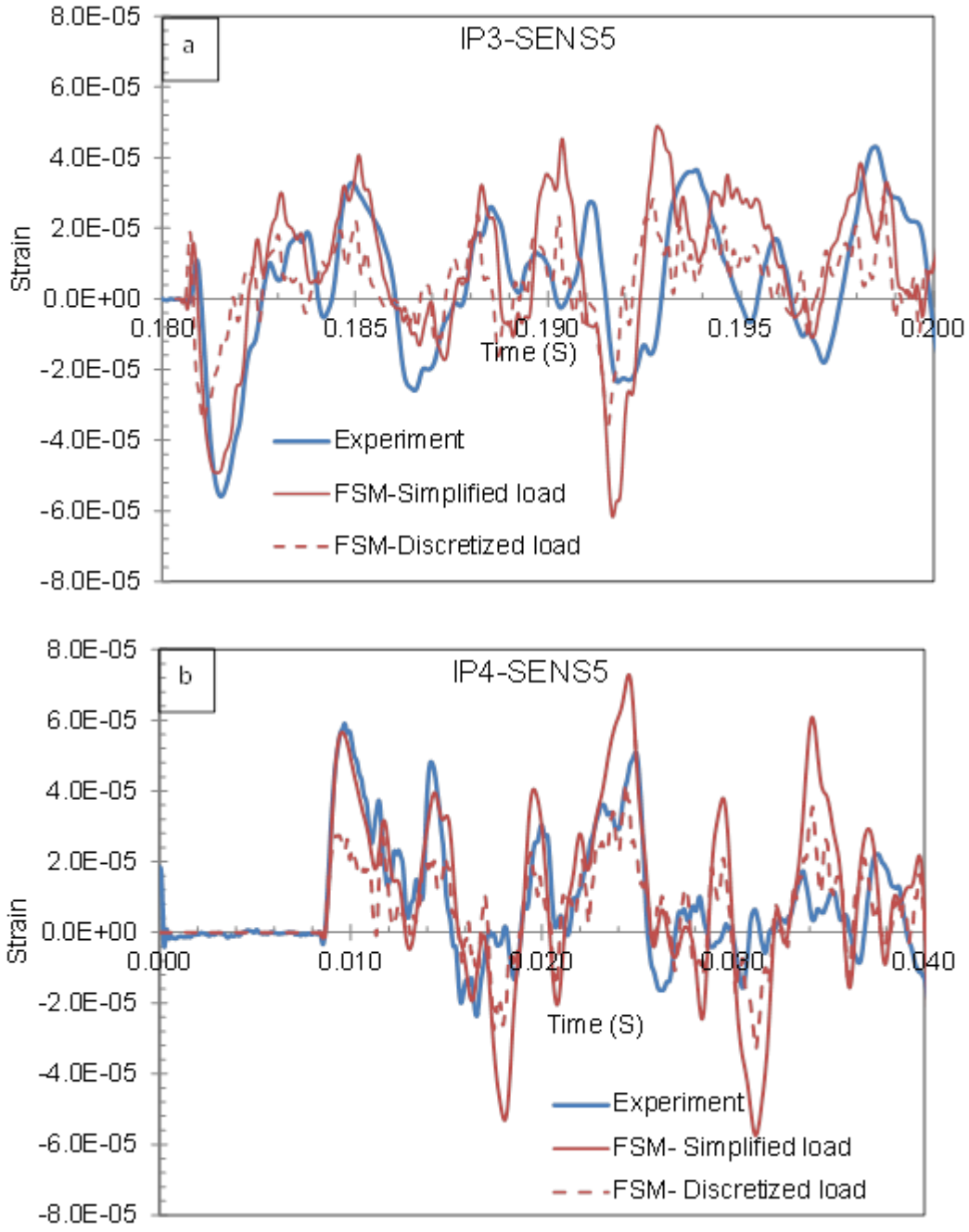

Figure 3.4 Comparison of strain time history obtained from the experiment and forward solving model (FSM) using the simplified (sinusoidal) and discretized loads at SENS5 location (see Figure 3.1) for impact at a) IP3 and b) IP4 locations

Another important factor with the FSM is the number of modes used in Eq. (3.6) to predict strain in a plate. Practically higher modal frequencies have insignificant contributions to the total response of the structure and can be ignored for computational efficiency. To find the frequency (mode) cut-off in Eq. (3.6), the number of modes considered in the computations is varied from 4 to 625 by changing the upper limit for "*i*" and "*j*" equally. This is equivalent to a frequency range between 0.45 and 69.85 kHz. Figure 3.5 shows that more than the plates' dominant frequencies (first few modes) have to be included in the

computations to achieve accurate results. Figure 3.5.a compares the strain at SENS5 location of the plate due to an impact at IP4 and with a different number of modes included in the analysis. There is a moderately slight change in the strain above 25 modes (5 modes along x- and y-direction, respectively) and the change for more than 49 modes is insignificant. Figure 3.5.b indicates that the NSE also changes insignificantly for the case of more than 49 modes (7 modes along x- and y-direction, respectively). The case of 7 by 7 modes contains a maximum frequency of 5.58 kHz. Therefore, 5 kHz seems sufficiently high as a cut-off frequency.

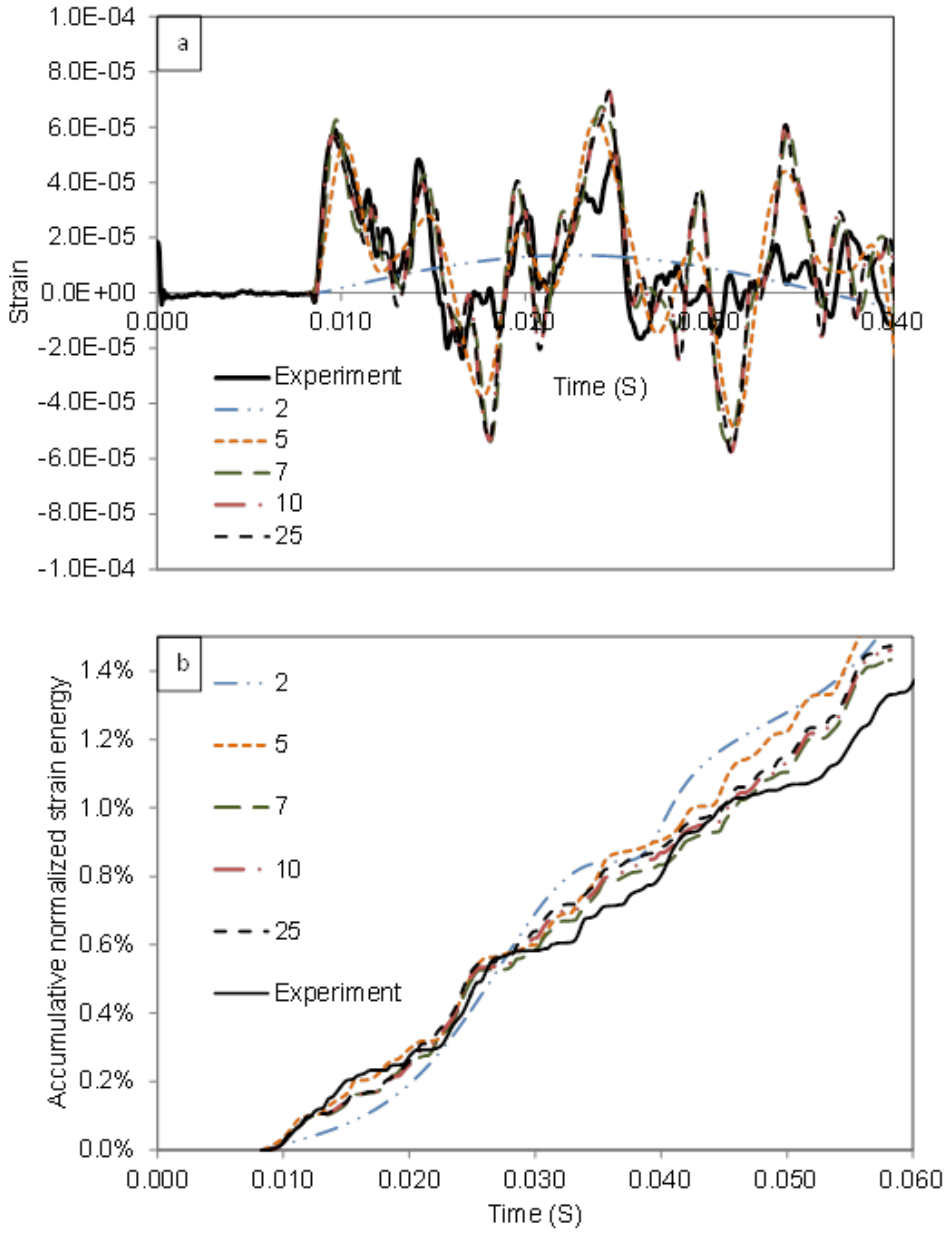

Figure 3.5 a) Effect of modal frequencies on the dynamic strain and b) normalized energy at SENS5 location for both FSM and experimental results due to impact at IP4 location (in FSM equal number of modes in *x*- and *y*-direction is considered, for instance 2 means 4 modes and 7 means 49 modes)

3.4 Verification of the inverse procedure

The three options discussed earlier for layers 1 and 2 of the system identification are verified with the experimental measurements of the IP3 and IP4 events and the best option for each layer is adopted for further analysis. For both cases, 2 and 5 kHz are considered as cut-off frequencies.

Layer 1

The results from layer 1 inverse analysis are summarized in Table 3.1.

Table 3.1 Summary of Layer 1 inverse analysis for the impact at IP4 and two cut off frequencies, 2 and 5 kHz, using the three options for layer 1 (the percentage in parentheses indicates the error in the coordinates with respect to the actual coordinates)

Time of Arrivals (S)				
Sensor	OPT1		OPT2	
	Frequency cut-off = 2 kHZ	Frequency cut-off = 5 kHZ	Frequency cut-off = 2 kHZ	Frequency cut-off = 5 kHZ
SENS4	286.825E-3	8.475E-3	286.250E-3	8.450E-3
SENS5	287.100E-3	8.700E-3	286.875E-3	8.700E-3
SENS7	286.900E-3	8.450E-3	286.325E-3	8.475E-3
SENS8	287.175E-3	8.500E-3	286.450E-3	8.625E-3

Dominant wave frequency		
Frequency cut-off (kHz)	2	5
Dominant frequency* (kHz)	0.017	0.019

Estimated impact Location							
Impact location coordinates	Target	OPT1		OPT2		OPT3	
		2 (32.5%)*	5 (38.6%)	2 (36.8%)	5 (26.8%)	2 (35.8%)	5 (26.8%)
ξ (m)	.465	0.51 (9.7%)	0.52 (11.8%)	0.52 (11.8%)	0.50 (7.5%)	0.51 (9.7%)	0.50 (7.5%)
η (m)	.339	0.36 (6.2%)	0.36 (6.2%)	0.35 (3.2%)	0.36 (6.2%)	0.37 (9.1%)	0.36 (6.2%)

*This error is ratio between the distance of the detected IL and the target point and the grid size.

The dominant frequency is far less than the considered cut-off frequencies and it does not change noticeably with the two experiments with different cut-off frequencies. The detected coordinates through the three options do not show a significant deviation from each other. Having the ratio between the distance to the actual IL and the grid size, option 1, 3, and 2, respectively, lead to the least to most accurate results when 2 kHz is used as the cut-off frequency. However, option 1 leads to the least accurate results when the cut-off frequency rises to 5 kHz. This indicates incapability of the threshold method when the signal noise level is high. Option 1 consists of the standard triangulation using the threshold method to determine TOA. Option 2 is similar except it uses integral of the signals to find TOAs. Figure 3.6 demonstrates the approximated TOA at SENS5 due to impact at IP4 through different methods. Figure 3.6.a demonstrates how TOA is obtained through the threshold method. Figure 3.6.b and 3.6.c show the signal integral at SENS5 due to the impact at IP4 and at 2 and 5 kHz cut off frequencies, respectively. The point where the slope of the spectrum changes abruptly is taken as TOA. The point corresponding to TOA in the strain integral time history (Figure 3.6.b and 3.6.c) is clearer than that in strain time history (Figure 3.6.a). It has to be noted that that although the two spectra in Figure 3.6.b and c

are obtained from the signals at the same location and due to the impact at the same point, they look different because they are obtained from two different experiments and impact load characteristics. Normalized and un-normalized (accumulative) signal energies are shown in Figure 3.7. Normalized signal energy varies linearly with time for any experiment but the un-normalized one is nonlinear which approaches to an asymptote toward the end of vibration. The un-normalized signal energy graphs for the experiments conducted at 2 kHz cut-off frequency are shifted to the origin because the impact start time is later than the other one and the noisy signal before impact event appears as almost zero energy on the spectrum. The rate of signal energy (signal power) is constant for the NSE and it is almost identical in both experiments (2 and 5 kHz cut-off frequencies). The normalized signal power might not be identical for the two experiments at the initial portion of the graph before TOA. For instance, TOA at SENS5 for the experiment with the 2 kHz cut-off frequency is 0.2871 s and the slope of the line before 0.2871 is different from that for the 5 kHz cut-off experiment. Therefore, normalized signal power (slope of the lines shown in Figure 3.7.a) is an appropriate parameter for localization since it is not significantly affected by noise. Additionally, normalized signal power (the slope of NSE line) is mainly dependent on IL rather than ILTH due to normalization. Therefore, it is a suitable alternative for layer 1 of the inverse analysis, which only seeks IL.

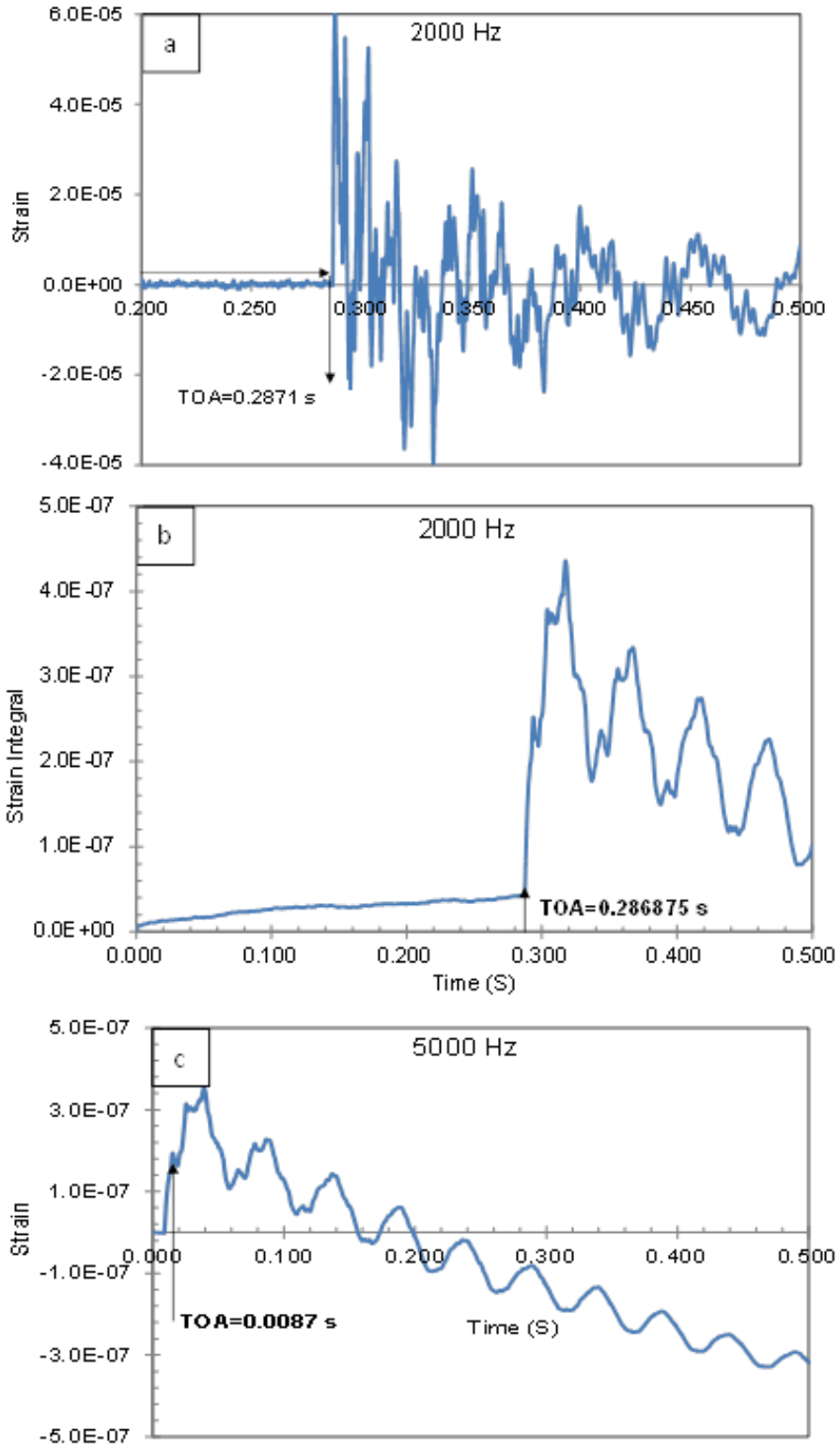

Figure 3.6 TOA determination in layer 1 inverse analyses using the signals obtained at SENS5 location due to impact at IP4 a) option 1 (threshold method), 2 kHz cut-off frequency, b) option 2 (strain integral), 2 kHz cut-off frequency, and c) option 2 (strain integral), 5 kHz cut-off frequency

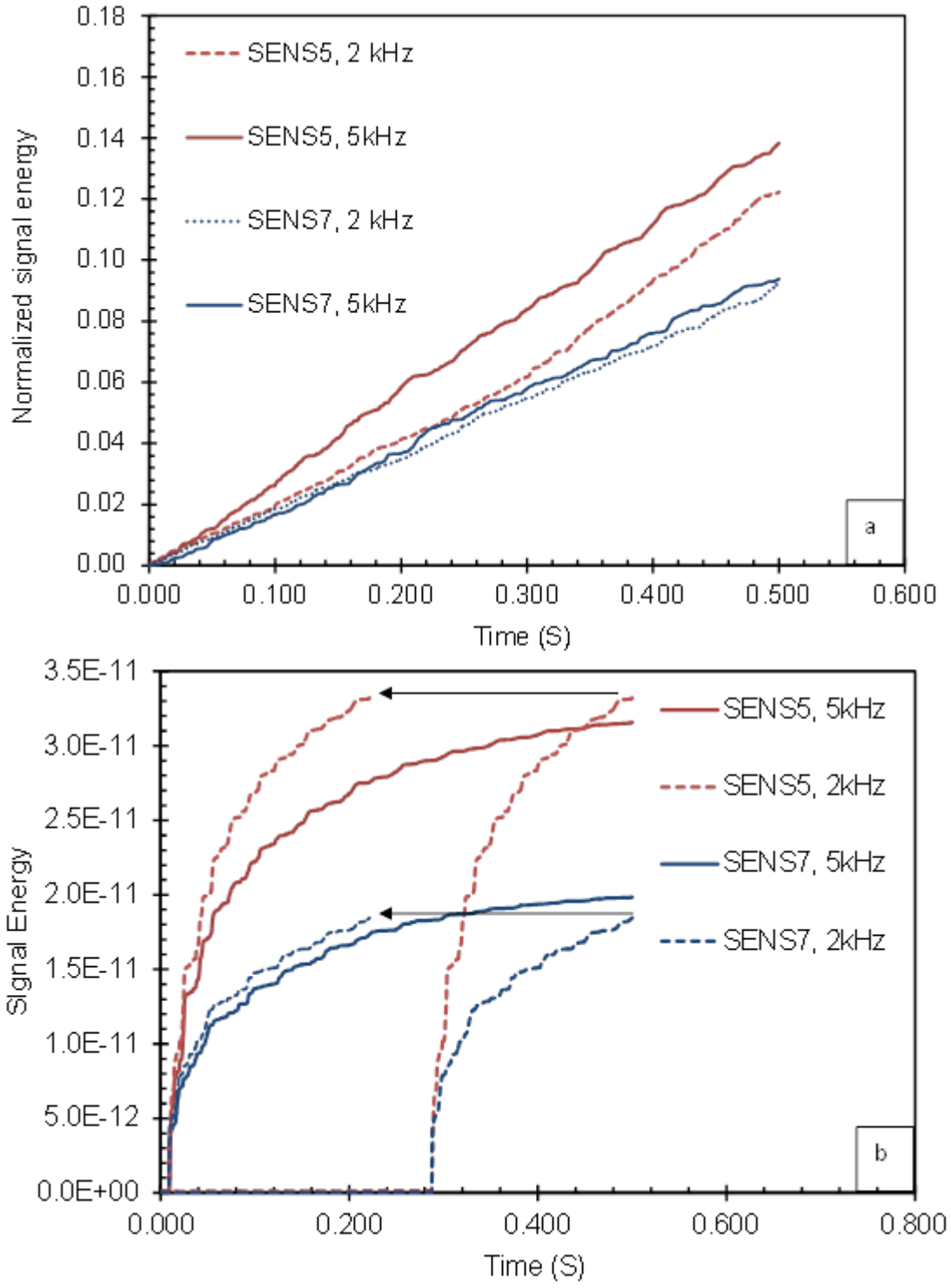

Figure 3.7 a) Normalized signal energy and b) signal energy for the two sensors at SENS 5 and SENS7 locations due to impact at IP4 obtained from two different experiments with 2 and 5 kHz cut-off frequencies

Layer 2

Layer 1 of the inverse analysis indicates that OPT3 is the most convenient and accurate method for IL estimation. Having the IL from layer 1, layer 2 of the inverse analysis is performed to refine the IL and find the impact amplitude and loading and unloading frequencies using the three options discussed above. Similar to layer 1, the experimental data for the IP4 event at 2 and 5 kHz cut-off frequencies is used as input for layer 2 inverse analyses. In all the analyses, about 70 data points from the experiment with a sampling frequency of 8 kHz is used. The IL coordinates estimated in layer 1 are used as the mean of the possible IL for layer 2 optimization procedure. The radius of the deviation is determined by the distance between the mean coordinates from layer 1 and coordinates of the gridlines. For example, layer 1 results in x-coordinate of 0.50 for IP4 at 5 kHz cut-off frequency (see table 1). $x = 0.50$ m is closer to the $x = 0.44$ gridline and hence the radius of the interval is $0.50 - 0.44 = 0.06$. Then the search interval is bounded between 0.44 and 0.56 (= 0.50 + 0.06). The impact amplitude is varied between 50 and 550 N, start time between 100 and 1000 μS, loading frequency between 500 and 2000 Hz, and unloading frequency between 100 and 1000 Hz, with 3, 3, 4, 3, 2, 2 sample points, respectively, which results in a total of 432 particles. In option 2, since the impact amplitude is determined through a different inverse procedure, the first sub-layer consists of 48 particles and the second sub-layer only 6 particles. This leads to a significantly faster computation since in heuristic optimization algorithms, the number of particles is important for computational efficiency. Since the experiment start time is arbitrary, for convenience, start time is assumed to be zero at the time when the farthest sensor in the grid is triggered, so t_0 is the TOA at the farthest sensor location. Since in OPT1 and 2, only three out of four sensors are used, t_0, according to the convention, is different from that of OPT3.

Table 3.2 compares the refined IL as well as the start time, the impact amplitude, and the impact momentum obtained from the experiments performed at IP4 with cut-off frequencies of 2 and 5 kHz and the ones back-calculated by the inverse analysis using the three alternatives. The error between the back-calculated and measured IL indicates that the data obtained from the 5 kHz experiment lead to more accurate results. In contrast, in layer 1, 2 kHz frequency cut-off lead to slightly more accurate ILs for OPT1. This is because the signal data are pre-filtered by using a lower cut-off frequency so that TOA can be found more conveniently in layer 1 of the inverse analysis; however, by using a lower cut-off frequency a large amount of information might be lost. In layer 2 of the inverse analysis, the magnitude of measurements is important for matching the predicted and measured signal data, a lower cut-off frequency would lead to less accurate results due to loss of the signal data.

Table 3.2 Summary of refined coordinates of IL and impact load characteristics for the impact at IP4 using different proposed options for layer 2 (the percent in the parentheses indicates the error)

	Actual		Cut-off Frequency (kHz)					
			2			5		
	2 kHz	5 kHz	OPT1	OPT2	OPT3	OPT1	OPT2	OPT3
ξ (m)	0.465	0.465	0.434 (26%)	0.486 (14%)	0.446 (33%)	0.457 (6%)	0.486 (14%)	0.439 (17%)
η (m)	0.339	0.339	0.315	0.337	0.385	0.342	0.336	0.343
t_0 (μS)	125 (OPT1&2) 550 (OPT3)	575(OPT1&2) 650 (OPT3)	990 (692%)	881 (605%)	937 (70%)	515 (10%)	611 (6%)	195 (70%)
F_0 (N)	133.4	148.6	71.6 (46%)	66.1 (50%)	294 (120%)	83.7 (44%)	76.3 (49%)	179.0 (20%)
Impact Momentum (N.mS)	81.8	71.9	111.7 (36%)	112.0 (37%)	86.3 (5%)	202.5 (182%)	110 (53%)	98.4 (37%)

The error percent shows that OPT3 results in the most accurate impact load amplitude for the 5 kHz cut-off frequency experiment. In an impact event, not only the amplitude but also the impact duration and other impact characteristics determine the severity of an occurred damage. From this point of view, the impact momentum is important to evaluate the likelihood of structural damage and its severity, which is calculated for all the back-calculated ILTHs and the corresponding measurements. It can be seen that the calculated impact momentum is the most accurate with OPT3. Reconstructed and the measured ILTHs are shown in Figure 3.8. In general, OPT3 leads to a better fit to the measured ILTH when cut-off frequency is sufficiently high. Therefore, it is adopted for further study in this paper.

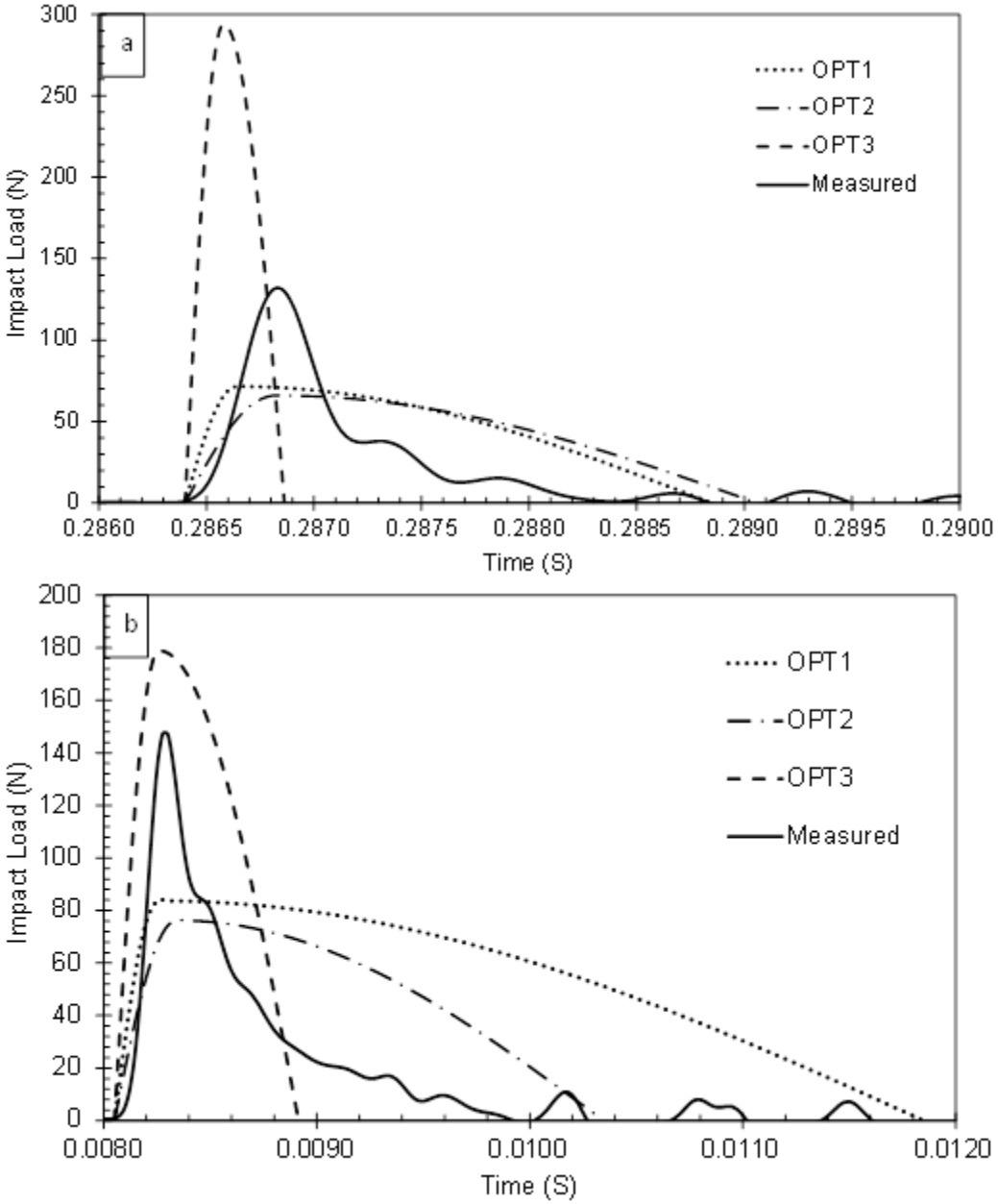

Figure 3.8 Comparison of the identified impact load time history (ILTH) through different options with the measured one from the experiment conducted at IP4 and with a) 2 kHz and b) 5 kHz cut-off frequency

3.5 Implementation of the modified inverse procedure

The experiment is repeated at other locations (Figure 3.1) with 5 kHz cut-off frequency, and then layer 1 and 2 of the inverse procedure are performed on the measurements to detect IL and reconstruct ILTH. OPT3 is adopted for layer 1 and OPT1 and OPT3 are used for layer 2. The identification results are shown in Figure 3.9 and 3.10 and Table 3.3. Figure 3.9 exhibits that despite the presence of system error, the impact location can be approximated using the proposed inverse procedure. Table 3.3 also shows that the impact load amplitude and impact momentum can be obtained with OPT3 of layer 2 with an acceptable precision. In general, OPT1 results in more accurate estimation of IL than OPT3. In contrast,

OPT3 results in more accurate estimation of the impact load amplitude and impact momentum. The main reason for the discrepancy is the error between the mathematical model and the experiment. Depending on the type of cost function used in the inverse analysis, the fitting procedure is guided toward certain unknowns. OPT1 minimizes the difference between the measured and predicted strains at sensor locations to find the unknown parameters while OPT3 minimizes the difference between the average signal powers. Average signal power is indicative of the impact energy received by the sensors and thus it is strongly correlated with the impact amplitude and impact momentum. On the other hand, although strain depends on both IL and ILTH, it exhibits weaker dependence on impact load amplitude than IL. The above-described interval analysis is used to find the error in IL and impact load amplitudes caused by system error, i.e., the error between the FSM and the experiment. A maximum system error of 5E-6 in strain is assumed for all the sensors. To solve Eq. (3.12) and find the deviation in the identification parameters due to the system error, the error in the signal power (the difference between analytical and experimental signal power) due to the system error has to be found first. The experimental signal power based on analytical strain and system error is:

$$P_i^e = \frac{\int_{t_i}^{t_f} (\varepsilon_i(t) + e)^2 \, dt}{t_f - t_i} = \frac{\int_{t_i}^{t_f} [\varepsilon_i^2(t) + e^2 + 2e.\varepsilon_i(t)] dt}{t_f - t_i} \tag{3.14}$$

Where t_f is the end sampling time; t_1 is the start sampling time; e is the strain system error; and $\varepsilon(t)$ is the analytical strain at time t.

Table 3.3 Identified impact load amplitude and impact momentum at different locations using OPT1 and OPT3 in layer 2 of inverse analysis

Impact location	Impact load amplitude (N)			Impact momentum (N*ms)		
	OPT1	OPT3	Target	OPT1	OPT3	Target
IP1	83.5	289.7	211.1	1230	96.1	85.2
IP2	70.8	148.8	127.0	127.9	72.3	59.7
IP3	68.4	191.4	144.1	106.1	64.2	65.2
IP4	83.7	179.0	148.6	202.5	98.4	71.9

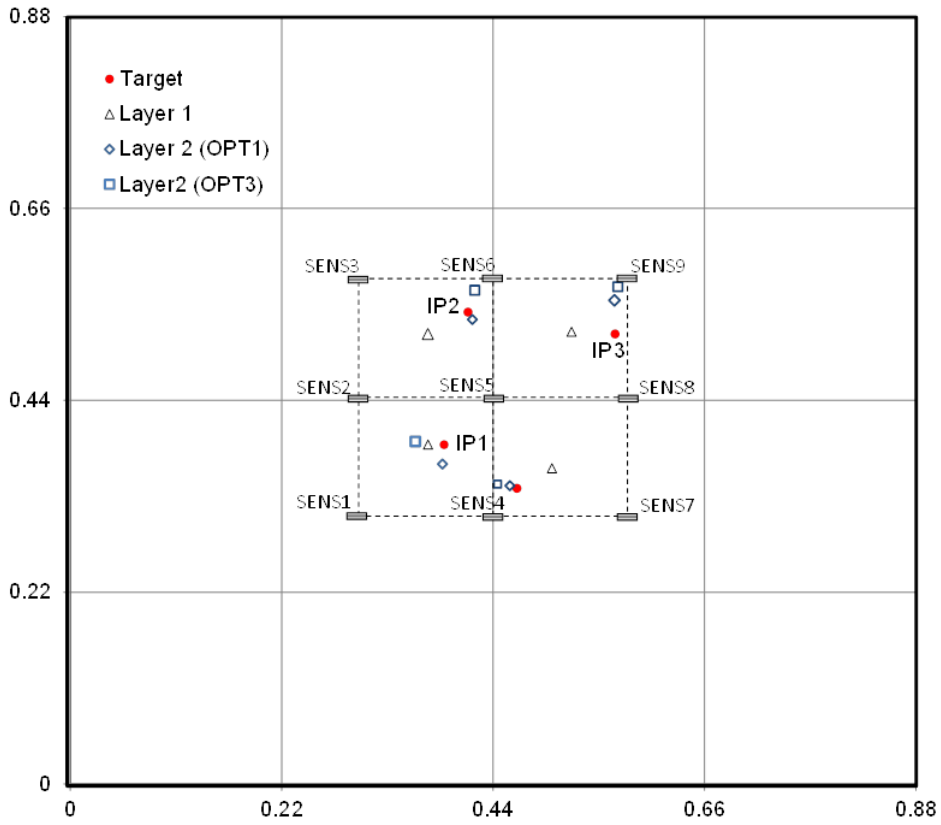

Figure 3.9 Detected impact location for the impact experiment at different locations based on layer 1 and layer 2 of the inverse procedure

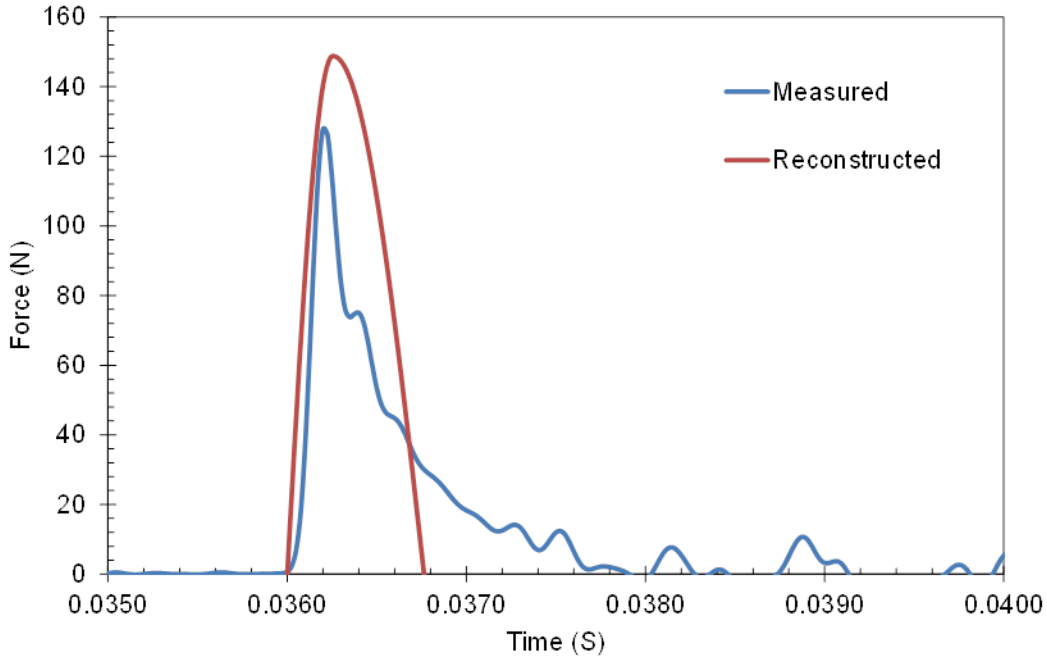

Figure 3.10 Reconstructed impact load time history with OPT3 for the impact experiment at IP2 and 5 kH cut off frequency

Therefore, error in the signal power is the difference between Eq. (3.14) and (3.10):

$$\Delta P = \frac{\int_{t_i}^{t_f} [e^2 + 2e \times \varepsilon_i(t)] dt}{t_f - t_i} \tag{3.15}$$

The error in the signal power can be calculated numerically by substituting Eq. (3.6) into (3.15). Having the error in signal power and signal data, Eqs. (3.11) to (3.13) are applied to find the deviations in the parameters due to the system error.

The computed deviations in the *x*- and *y*- coordinates of the ILs are plotted in Figure 3.11. It can be seen that the likelihood region of IL obtained by OPT1 is contained with that of OPT3, that is, OPT3 is more likely to result in less accurate IL. Table 3.4 compares the computed deviations in impact load amplitude for the two options. System error causes a smaller error to amplitude for OPT 3. Table 3.2 and 3.4 are consistent because Table 3.2 shows that the IP4 experiments result in the most precise impact amplitudes with OPT3 and Table 3.4 shows that IP4 has the narrowest range of impact load amplitudes.

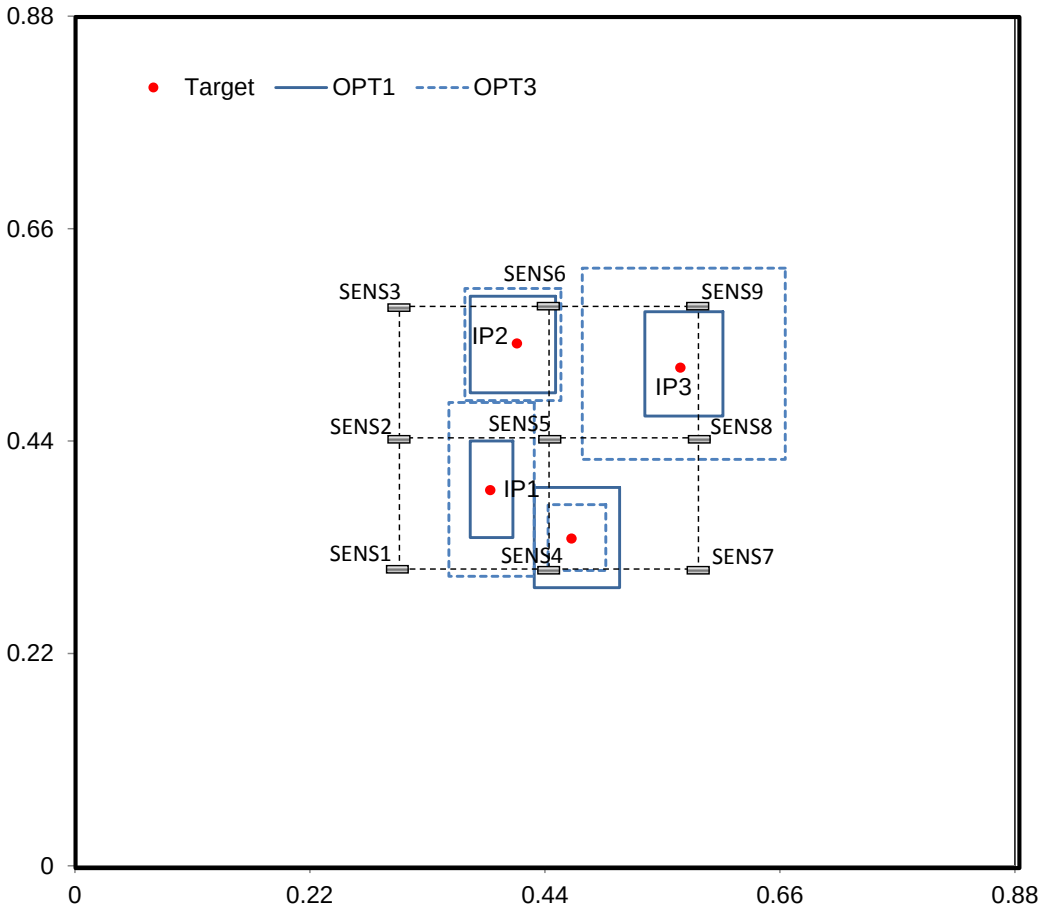

Figure 3.11 Comparison between the deviations in the estimated impact location due to an assumed system error (the error between the model and the experiment) through OPT1 and OPT3 inverse analysis

Table 3.4 Deviations in the impact load amplitude due to a system error of 5E-6 in strain for OPT 1 and 3 and different impact locations

	IP1	IP2	IP3	IP4
OPT1	40	33	38	39
OPT3	38	18	25	12

3.6 Linearity of normalized signal energy

In this study, a new parameter, normalized signal energy (NSE), was introduced for layer 1 of the inverse problem. It was shown in Figure 3.7 that NSE grows linearly with time while un-normalized signal energy changes nonlinearly. The rate of change of NSE (slope of the line) was adopted as the system characteristic to estimate IL. To understand the reason why the NSE is linear with time and the associated limitations, Eq. (3.6) is rewritten as following by representing the mode shape by A^{L}_{ij} and amplitude by $G_{ij}(t)$:

$$\varepsilon(t) = \sum_{i=1}^{m}\sum_{j=1}^{n} A^{L}_{ij} G_{ij}(t) \tag{3.16}$$

where L denotes the sensor location. Assume that the impact load is a sinusoidal function with equal loading and unloading frequency. Although, this is not the case in practice, the generality of the conclusion would not be affected. Then $G_{ij}(t)$ is:

$$G_{ij}(t) = \frac{\sin(\omega t)}{2(\omega+\omega_{ij})} + \frac{\omega\sin(\omega_{ij} t)}{2(\omega^2+\omega^2{}_{ij})} = a_{ij}\sin(\omega t) + b_{ij}\sin(\omega_{ij}) \tag{3.17}$$

Substituting Eq. (3.16) and (3.17) into Eq. (3.3) and assuming four sensor locations are used, we have:

$$\varepsilon^{n}_{L}(t) = \frac{\{\sum_{i=1}^{m}\sum_{j=1}^{n} A^{L}_{ij}[a_{ij}\sin(\omega t) + b_{ij}\sin(\omega_{ij} t)]\}^2}{\sum_{L=1}^{4}\{\sum_{i=1}^{m}\sum_{j=1}^{n} A^{L}_{ij}[a_{ij}\sin(\omega t) + b_{ij}\sin(\omega_{ij} t)]\}^2} \tag{3.18}$$

Eq. (3.18) is a periodic function, which varies between 0 and 1, and since square of the sine functions appears in the equation, its frequency content consists of double of impact load frequency (2ω) and the plate modal frequencies ($2\omega_{ij}$). There is no closed form solution to the integral in Eq. (3.18). Since $\varepsilon^{n}_{L}(t)$ is always positive and oscillating between 0 and 1 at high frequencies, the area under it increases almost linearly when time duration is long as evidenced in Figure 3.5.b and 3.7.a. Therefore, if duration of vibration is long enough, the NSE is close to a line. To ensure the linearity of NSE, integration time has to be sufficiently larger than the largest period of oscillation, which is $1/2f_{min}$, where f_{min} is the smallest vibration frequency. For the given plate above, the smallest frequency is 114.1 Hz, so duration of vibration has to be longer than 0.004 s, which is much shorter than 0.5 s considered in the calculations.

Un-normalized signal power is:

$$\varepsilon_L^n(t) = \{\sum_{i=1}^{m}\sum_{j=1}^{n} A_{ij}^L[a_{ij}\sin(\omega t) + b_{ij}\sin(\omega_{ij} t)]\}^2$$
$$= \alpha\sin^2(\omega t) + \alpha_{11}\sin^2(\omega_{11} t) + ... + \alpha_{mn}\sin^2(\omega_{mn} t) + 2\alpha\alpha_{11}\sin(\omega t)\sin(\omega_{11} t) + ... \quad (3.19)$$

Integration of Eq. (3.19) yields:

$$\int_0^t \varepsilon_L^{n^2}(t) =$$
$$\alpha[\frac{t}{2} - \frac{\sin(2\omega t)}{4\omega}] + \alpha_{11}[\frac{t}{2} - \frac{\sin(2\omega_{11} t)}{4\omega}] + ... + 2\alpha\alpha_{11}\{\frac{\sin[(\omega-\omega_{11})t]}{2(\omega-\omega_{11})} - \frac{\sin[(\omega+\omega_{11})t]}{2(\omega+\omega_{11})}\} + ... \quad (3.20)$$

In Eq. (3.20), since frequencies are typically high (over 100 Hz in this study), all the sinusoidal terms can be ignored if duration *t* is sufficiently long. Therefore, un-normalized signal energy is linear with time theoretically; however, it did show in Figure 3.7.b due to damping effect. Instead un-normalized signal energy increases with time until it flattens toward the end of vibration. This does not apply to the NSE because, although the rate of change in power decreases with time, the normalized power still oscillates between 0 and 1 and it never decays away. In Eq. (3.20), in order to eliminate the high frequency data effect on un-normalized energy, as mentioned, *t* has to be sufficiently large or $2\omega t >> \sin(2\omega t)$. With $\omega = 2\pi \times 114$, duration longer than 0.013 s ensures the dominance of *t* in Eq. (3.20). The computations presented above satisfy both time restrictions.

3.7 Conclusions

An experimental study was conducted to evaluate the impact location and impact load identification proposed.[40] In layer 1, impact location (IL) was estimated then it was refined in layer 2 and also impact load time history (ILTH) was reconstructed. To maximize effectiveness and efficiency of the inverse algorithm, different options were proposed for each layer. A new parameter, normalized strain energy (NSE), was introduced as an option for layer 1 and it was adopted throughout the study for its convenience and accuracy since it does not require finding time of arrival (TOA). Measurement error was minimized by pre-filtering using low-pass filter. The study indicated that 5 kHz is sufficient as cut-off frequency. With lower cut-off frequency, due to loss of data, inaccurate results were obtained. System error, the discrepancy between the forward solving model (FSM) and the real structure, causes error in the identification parameters. Therefore, different options were evaluated for layer 2 and it was concluded that using the difference between the predicted and measured strain as cost function leads to more accurate results in terms of IL, but using signal energy in cost function leads to more accurate results in impact load amplitude. Depending on the importance of the unknowns, one of the options may be adopted. A new cost function combining the two options would improve accuracy of IL and impact load amplitude; however, a normalization factor is needed to balance the effect of both strain and power in the objective function. This was not considered in this study in order to not compromise simplicity of the proposed inverse scheme.

4. IMPLEMENTATION OF THE INTEGRATED SHM AND IMPACT/COLLISION SYSTEM IN FIELD

4.1 Introduction

A bridge located approximately 15 miles (1609.3 m) northwest of Fargo, ND, was load tested. In order to correctly rate the bridge and further validate a hypothesized structural health monitoring methodology-displacement distribution-based structural health monitoring, a two dimensional "grillage method" is used to idealize the longitudinal and transverse stiffness of the deck and beams in a grid system. The developed model was first verified using the field data obtained from Bridge Diagnostics, Inc. (BDI). Based on the field test results, a deformation distribution-based bridge health monitoring methodology is suggested, which could relate the deformation measurements at several locations of the bridge with the structural health status of the bridge, or directly with the ratings of the bridge.

The bridge is a single span beam-slab bridge with an overall length of 60.0 ft. (18.3 m) and a clear span of 57.0 ft. (2.1 m). The superstructure is composed of five post-tension concrete I-beams and two intermediate diaphragms made of reinforced concrete. The deck is made of 6.0 in. (0.15 m) reinforced concrete with a small curb and steel railing along the edges. Figures 4.1-3 show in detail the dimensions of the bridge and the I-beams, in terms of the bridge plan view, bridge cross-sectional dimensions, and the typical I-beam dimensions, respectively.

The grillage model was first developed and compared to the field test data and was found to match well. Several damage cases were then simulated to analyze the change in the bridge's structural responses due to them. With the results from damage simulations, ratios between the relative deflections of different locations were then extracted to quantify the level of the damages and their locations.

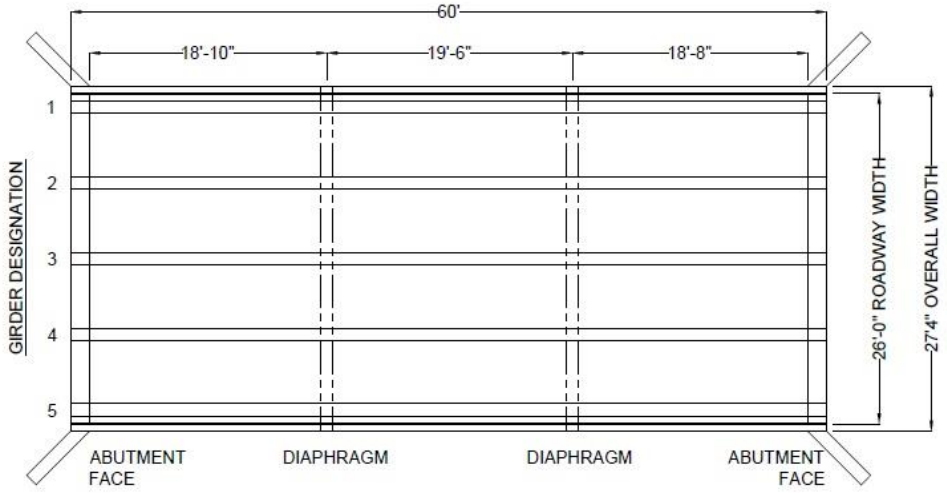

Figure 4.1 Plan view of the bridge (All numbers in ft-in)

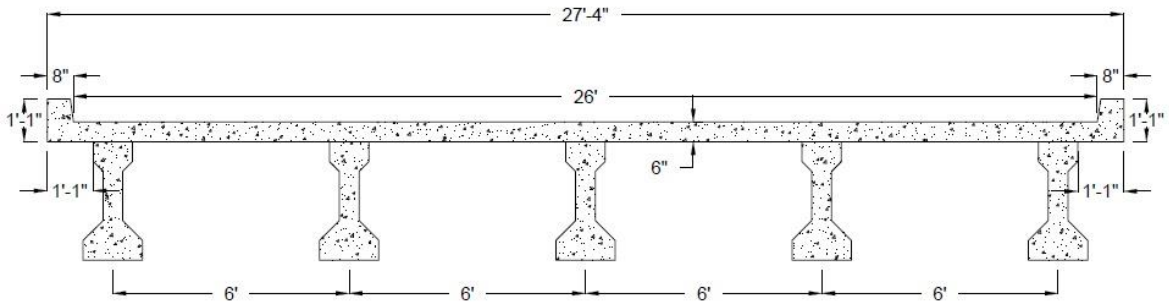

Figure 4.2 Cross-sectional view of the bridge (All numbers in ft-in)

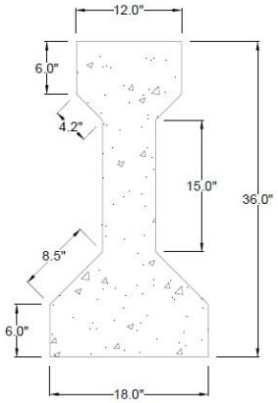

Figure 4.3 Typical I-beam dimensions (All numbers in in.)

4.2 Load testing and data

The Cass County 32 bridge was tested by Bridge Diagnostics, Inc. (BDI) using a total of 40 sensors placed at three cross-sections of the bridge.[41] Of the 40 sensors, there were 28 surface-mounted strain transducers, five cantilevered displacement sensors, and six tiltmeter rotation sensors. The displacement sensors were placed only at the cross-section B-B at midspan and the rotation sensors were placed at each end of beams 3 and 5. The strain sensors were placed on the bottom flange of all the post-tensioned beams at all three cross-section locations. For all the beams at midspan, a strain sensor was placed on the top flange as well as at the end cross-sections of beams 3 and 5. Additionally, four strain sensors were placed on the top and bottom of the curb to monitor its response and determine if it was contributing structurally to the bridge. A detailed arrangement of the sensor deployment can be seen in Fig. 4. Fig. 5 shows the sensor layout at each of the three cross-sections. The sensors used for this load test are standard sensors typically used by BDI, which can be viewed in detail at their website (www.bridgetest.com).

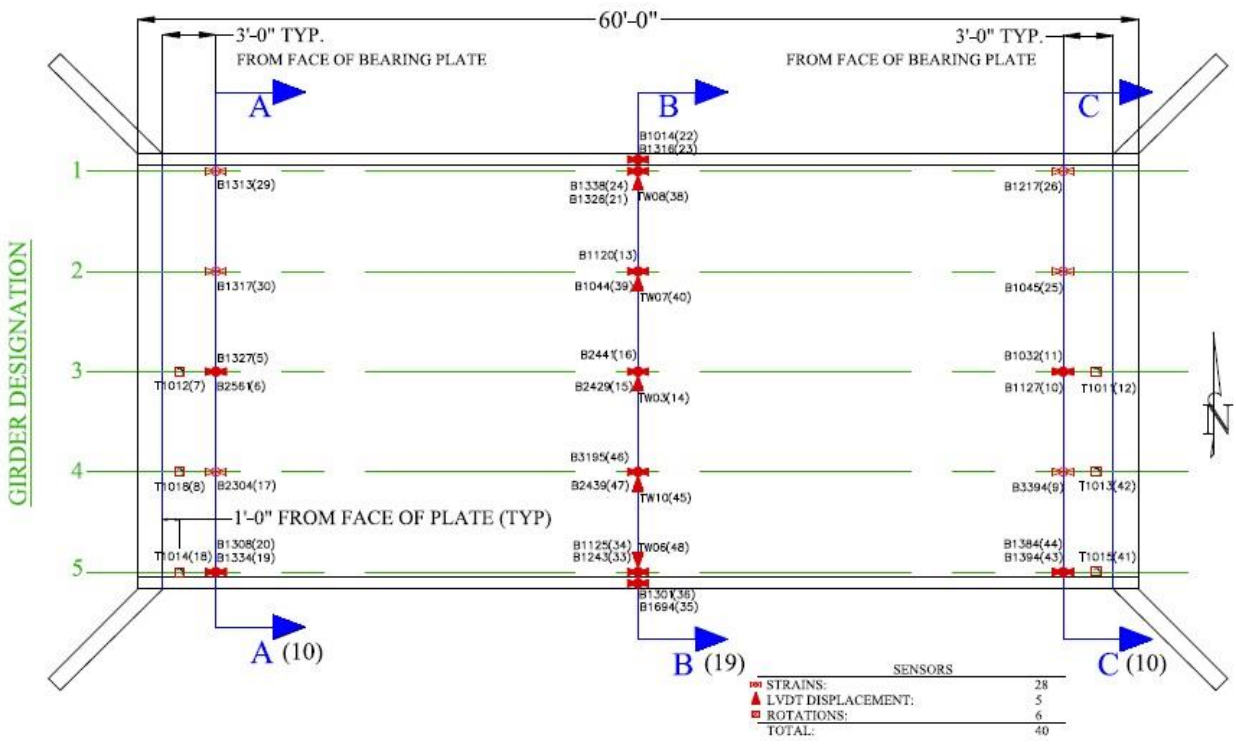

Figure 4.4 Sensor layout (BDI, 2012)

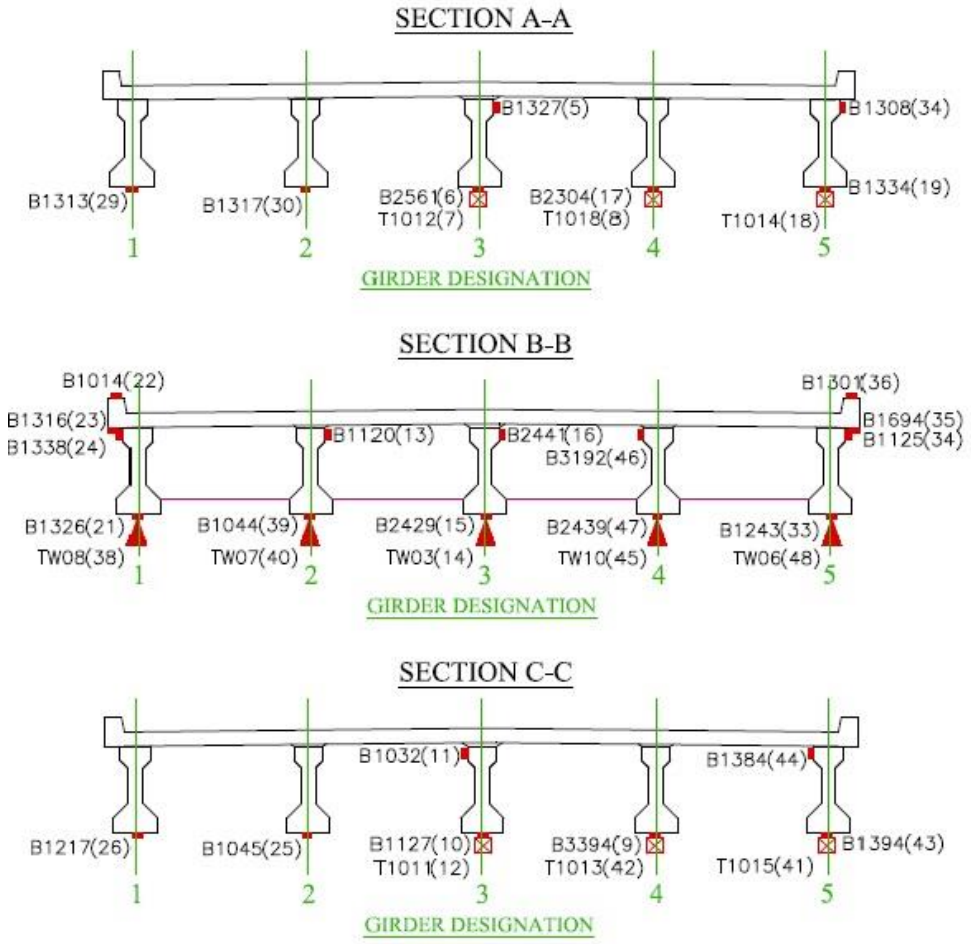

Figure 4.5 Cross-Sectional view of senor layout

To accurately measure the structural response of the bridge, three different load paths were used, referred to as Path Y1, Y2 and Y3. The location of each load path can be seen in Figure 4.6 below. Cass County Public Works provided a standard 48.0 kips (2.1x106 N) dump truck, which traveled over the bridge at 3-5 mph (1.3-2.2 m/s). The rear wheel on the passenger side of the truck was equipped with a sensor to monitor the location of the truck with respect to time as it passed over the bridge. The truck location was recorded simultaneously with the data from the sensors attached to the wheel so that the structural response data could be presented with respect to the truck location.

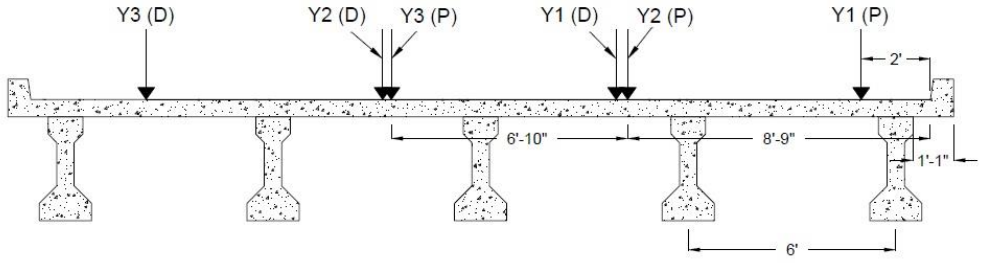

Figure 4.6 Lateral location of truck paths Y1, Y2, and Y3 (P stands for the passenger side, D stands for the driver side)

The truck passed over each load path twice to ensure a reliable data set was obtained for the analysis. In addition to passing over the bridge slowly, one additional dynamic load test over Path Y2 was conducted at a speed of 35 mph to measure the dynamic load effect.

After recording the raw data from the sensors, BDI processed the data using its own software program. The results were then evaluated by its engineers to ensure the data were of good quality. This was shown by having the strain measurements return to zero after loading and good reproducibility of responses. The strain measurements returning to zero after loading is also a good indication of elastic behavior of the beam. BDI also investigated the neutral axis depth from the strain measurements, and the depth was found to be fairly consistent throughout each beam. This is also an indicator of elastic behavior, which makes modeling of the bridge a less complicated task. Figure 4.7 below shows the strain results from three sensors for the two tests of each load path. Similarly, Figure 4.8 shows deflection results.

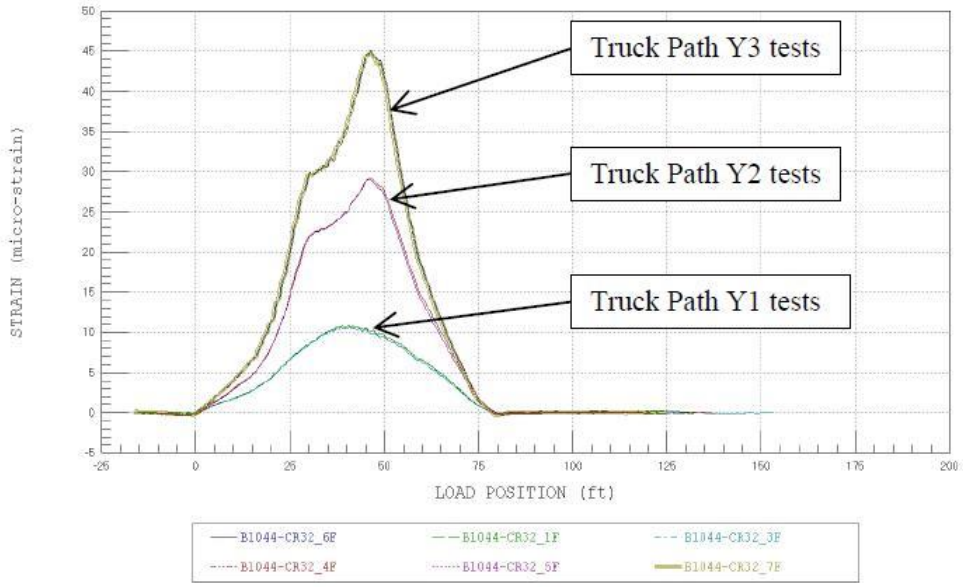

Figure 4.7 Strain Response Reproducibility (BDI, 2012)

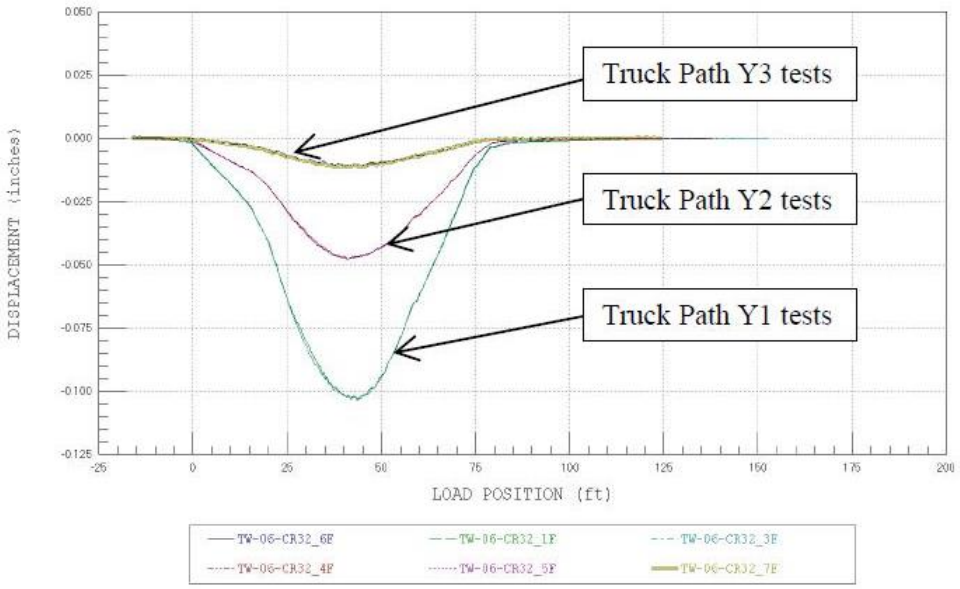

Figure 4.8 Deflection Reproducibility (BDI, 2012)

A typical strain response of the bottom flange at midspan can be seen in Figure 4.9. The figure shows the recorded strain responses of the bridge under the Y1 load path. As expected, beam 5 experienced the largest strain responses from the truck load and the level of strain decreased from beam 4 to beam 1. Since beams 1 and 2 experienced noticeable strain response, one can see that the diaphragms and deck to some level transfer the load laterally. The maximum strain occurs when the truck's front axle is approximately 45.0 ft (13.7 m) from the beginning of the bridge. This is also when the truck's second axle is approximately located at the midspan of the bridge. The positive strain values show that the bottom flange is in tension.

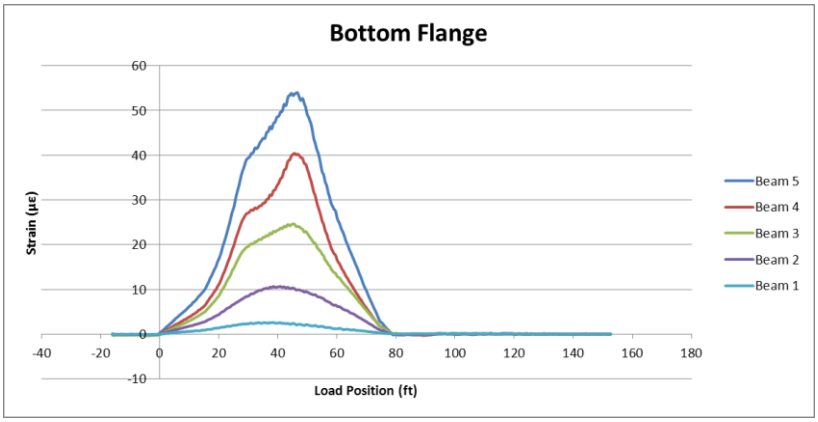

Figure 4.9 Midspan strain responses from load path Y1

Figure 4.10 shows a typical strain response of the top flange of the beams at midspan. Like the responses of the bottom flange, the largest response is seen at beam 5 with decreasing responses from beam 4 to beam 1. The localized spikes in strain that can be predominately seen in the beam 5 data and to a lesser extent in the beam 3 and 4 data; this is the result of the truck axle passing directly over the strain sensor location.

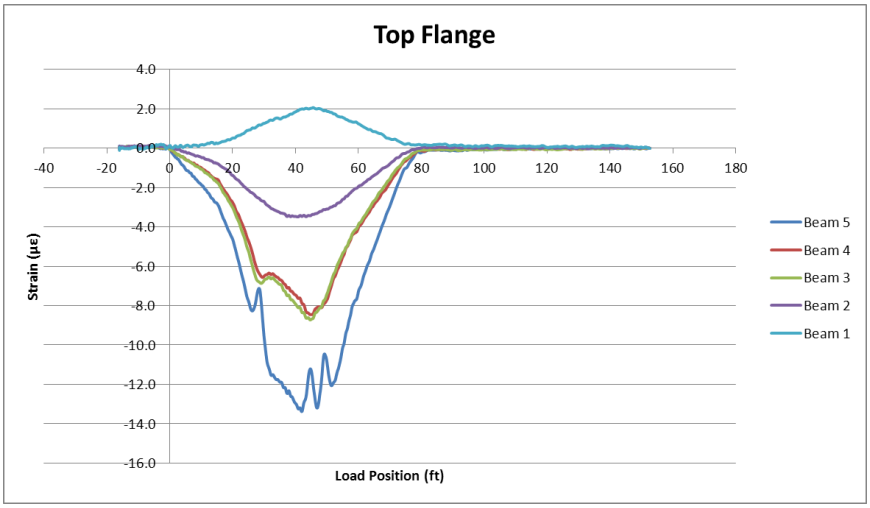

Figure 4.10 Midspan strain responses from load path Y1

Figure 4.11 shows the strain comparison of the top and bottom flange of beam 5. It can be seen that the top flange is in compression and the bottom flange is in tension. The large difference in magnitude between the two flanges and the similar shape of the response shows that the deck and beams are in composite action. The fact that the top flange experiences such smaller compression strains compared with the bottom flange tension strain indicates that deck slab is sustaining most of the compression strain.

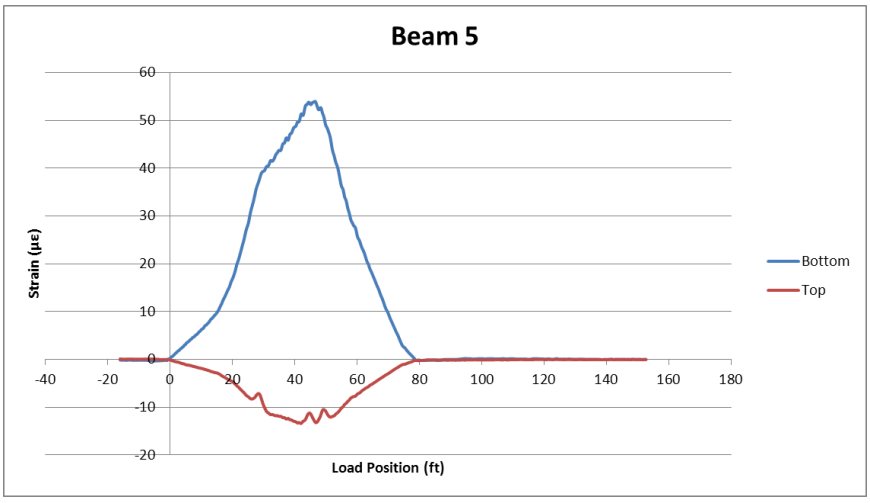

Figure 4.11 Observed composite behavior

Figure 4.12 shows the measured displacement at midspan of beams 1-5. The displacement measurements for all beams return to zero after loading, which indicates elastic behavior for the whole structural system. As expected, the greatest displacement observed was at beams 4 and 5, which are closest to load path Y1. Also, the maximum displacement occurs when the truck's front axle is located approximately 42.0 ft

(12.8 m) from the start of the bridge. At that location, the second axle is passing over the midspan of the bridge, the resultant force from the truck load is at this location.

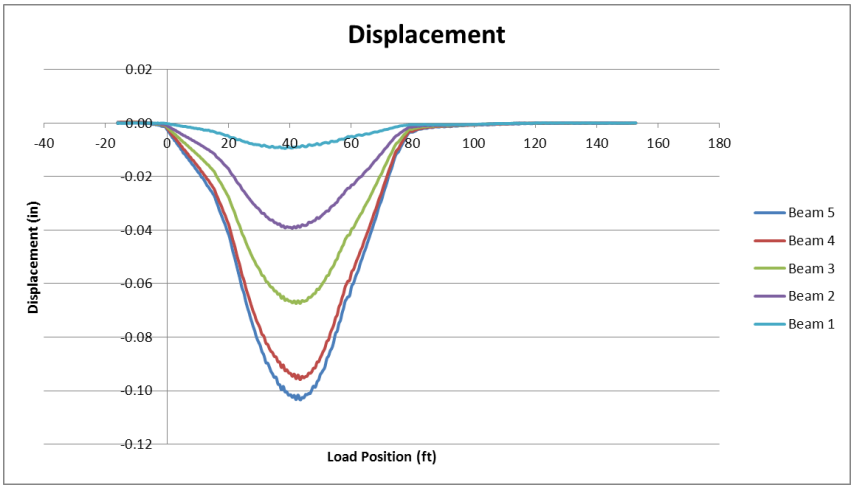

Figure 4.12 Example measured midspan displacement from load path Y1

With the load test data provided by BDI, a series of analytical models can be developed to investigate the bridge structure. With an accurate model, simulations of a compromised structure can be developed and analyzed to show the reliability of the proposed structural health monitoring technique with varying levels of damage.

4.3 Damage detection in bridges through Finite Element Modeling of its responses under loading

The Grillage method is a simple modeling method used to represent the stiffness of the deck through longitudinal and transverse beams. This method is commonly used among state DOTs to quickly analyze a simple beam-slab bridge structure. Typically, the longitudinal beams are placed where the actual bridge girders are located. The stiffness of these beams and the effective width of the deck are combined to give an approximate effective stiffness. Transverse members are placed at about 1.5 times the spacing of the longitudinal members. It is recommended that the spacing ratio not exceed 2:1. Transverse members should also be placed where any diaphragms are located. The stiffness of the transverse members is the transverse stiffness of the bridge deck. At locations where there is a diaphragm, the stiffness of both the deck and the diaphragm should be calculated (Jaeger and Bakht, 1982).[42]

The finite element program Abaqus was used to develop the grillage model. Five longitudinal beams were used to idealize the longitudinal stiffness of the bridge. The locations of these beams are where the actual bridge girders are located, which are spaced at 72.0 in. (1.8 m) on center. Five transverse beams were used to idealize the transverse stiffness of the bridge, two of which are placed at the diaphragms. The transverse beams were spaced at 117.0 in. (3.0 m) on center. The end boundary conditions were initially set as completely fixed, which was determined from visual observation of the beams' end conditions at the site. The end of the bridge girders were set on the abutments and had been fully grouted. However, soil movement behind abutments also contributes to bridge end boundary conditions. After comparing the results from the fixed boundary condition model with the actual field measurements, it was realized that the end boundary conditions need to be relaxed in order to mitigate the displacement difference. An axial spring and a rotational spring were added at each end of the beams. The results from the model matched with the field data after this change. It must be pointed out that the exact boundary condition is impossible

to obtain and not necessary as well, since the objective of the grillage model is to capture the relative stiffness distribution over the bridge layout. Figure 4.13 shows the basic layout of the bridge model.

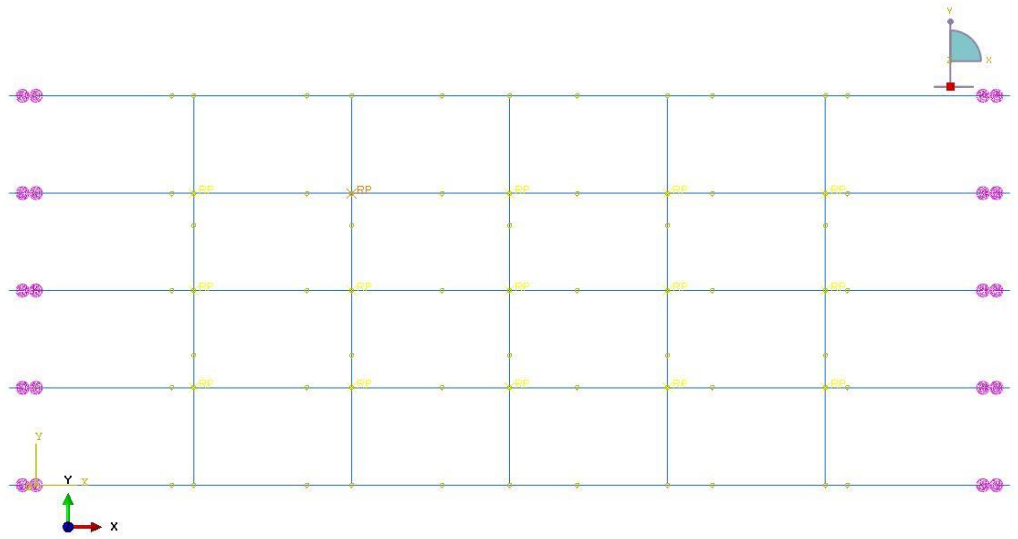

Figure 4.13 Grillage model layout

The calculations for idealized stiffness of both the longitudinal and transverse members were completed using an effective stiffness equation, which took the contribution of the reinforcing steel into consideration. The Young's modulus for the deck concrete and beam concrete was calculated using Eq. (4.1) and f_c' = 4500 psi (31.0 MPa) and 5500 psi (38.0 MPa) for the deck and beam respectively. The concrete strength of the bridge deck and girders were taken from BDI's final report on the bridge and represents an effective value of the field concrete strength through non-destructive testing.

$$E_C = 57000\sqrt{f_c'} \tag{4.1}$$

With the Young's modulus of the beam and deck, the combined modulus was calculated using Eq. (4.2). Based on the BDI's Ground Penetrating Radar (GPR) inspection of the deck, it was found that the reinforcement spacing for the top and bottom of the deck in the longitudinal direction was 16.0 in. (0.4 m) and 12.0 in. (0.3 m), respectively. For the transverse direction, both the top and bottom reinforcement spacing was found to be 12.0 in. (0.3 m). It was assumed that #4 bar was used for the reinforcement. For the post-tensioned beams, there are three ducts for the post-tension wires which each mostly likely hold 22, 0.25 in. (0.006 m) wires. There are also two reinforcement bars set in the top flange of the post-tensioned beams; for the calculation these were assumed to be #6 bar.
For longitudinal members,

$$E_{rc} = E_{c,eff} \times \left(1 + \frac{(A_{st,deck} + A_{st,beam}) \times \frac{E_S}{E_c}}{A}\right) \tag{4.2}$$

$$E_{c,eff} = \frac{(E_{beam} \times A_{beam}) + (E_{deck} \times A_{deck})}{A} \tag{4.3}$$

For transverse members,

$$E_{rc} = E_c \left(1 + \frac{A_{st,deck} \times \frac{E_S}{E_c}}{A}\right) \tag{4.4}$$

At diaphragm,

$$E_{rc} = E_c\left(1 + \frac{(A_{st,deck} + A_{st,diaph}) \times \frac{E_s}{E_c}}{A}\right) \tag{4.5}$$

E_{rc} is the Young's modulus of all the components combined together, including the concrete and reinforcing steel.

During the modeling process it was required to define a section for the longitudinal and transverse members. When defining the beam section, the parameter of the neutral axis is required. With the longitudinal members being a composite section of the beam and deck, the strain measurements from the field test data could be used to estimate the actual neutral axis depth. The following equation was used to determine the neutral axis depth at each data point.

$$E_{rc} = 36" + \left(\varepsilon_{tf} + \frac{36"}{\varepsilon_{bf} + \varepsilon_{tf}}\right) \tag{4.6}$$

Considering the beams are 36.0 in. (0.9 m) deep and the deck has a thickness of 6.0 in. (0.15 m), only the data points that produced a value in the range of 15.0 in. (0.4 m) to 36 in. (0.9 m) were considered further. The neutral axis location values were averaged combining all measurements at the three cross-sections and load paths. An overall average value for an interior beam and exterior beam was finally produced. A value of 26.2 in. (0.7 m) and 27.1 in. (0.7 m) was produced for the interior beams and exterior beams, respectively, measured from the bottom of the beam. These values are reasonable considering the beams and deck act as a composite section. For comparison purposes the neutral axis depth was calculated by hand for a typical interior beam and exterior beam. The calculated value for the interior beam and the exterior beam were 28.3 in. (0.72 m) and 26.8 in. (0.68 m), respectively. This comparison shows that there is composite action between the beam and deck, and also the values produced from the field data are reasonable.

Initially, the model's end support conditions were fully fixed because of reasons discussed earlier. After analysis and adjusting parameters of the beams it was found that changing the end conditions by adding an axial and rotational spring at each end of the longitudinal members worked well. This allowed the beams to translate longitudinally and rotate about the transverse axis. The stiffness values of the springs were adjusted individually until the best possible match with the field results was obtained. After the adjustment, displacement values from the model matched well with the field data in most locations under different loading paths. The stiffness values for each spring are shown in Table 4.1.

Table 4.1 Stiffness values for springs

Location	Axial Spring, West, kip/in (N/m)	Axial Spring, East, kip/in (N/m)	Rotational Springs, kip/in (N/m)
Beam1	1 (5.7)	1 (5.7)	1 (5.7)
Beam 2	1020 (5814)	528 (3010)	480 (2736)
Beam 3	762 (4343)	398 (2269)	362 (2063)
Beam 4	1116 (6361)	578 (3295)	525 (2993)
Beam 5	2125 (12113)	1100 (6270)	1000 (5700)

To simulate the truck moving across the bridge, concentrated loads were applied where the wheels were located and moved in 3.0 ft. (0.91 m) increments. Since load paths are not aligned with the girder lines, a transformation from the load points to the grillage nodes is needed. Figure 4.14 represents one section of the grid and Eqs. (4.7) - (4.12) show the methodology used. The wheel load location, P, is the actual location of the truck tire. P1 and P2 are the linearly distributed loads from P to the transverse members, which are then linearly distributed again to the four corners. The moment induced in the longitudinal direction by transferring the wheel load to the transverse members (P1 and P2) was neglected in the analysis because the error created is small and can be ignored. The moment induced in the transverse direction by transferring P1 and P2 to the four nodes was also ignored because there is no cantilever type loading in the model and most of the wheel lines are less than 2.0 ft. (0.61 m) from the nearest longitudinal member. For these reasons the error in both the longitudinal and transverse directions should be negligible (Jaeger and Bakht, 1982).[42]

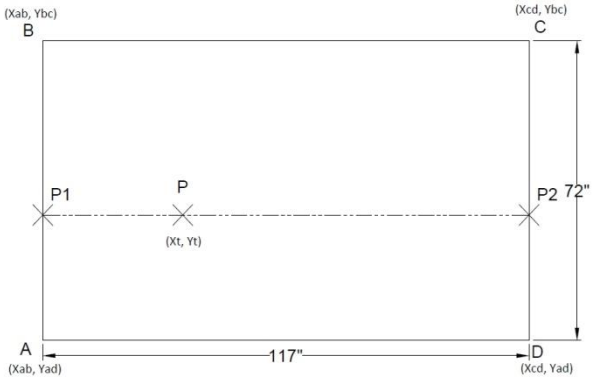

Figure 4.14 Truck load redistributed to member intersections

$$P_1 = P\frac{X_t - X_{ab}}{117"} \quad (4.7)$$

$$P_2 = P\frac{X_{cd} - X_t}{117"} \quad (4.8)$$

$$P_A = P_1\frac{Y_{bc} - Y_t}{72"} \quad (4.9)$$

$$P_B = P_1\frac{Y_t - Y_{ad}}{72"} \quad (4.10)$$

$$P_C = P_2\frac{Y_t - Y_{ad}}{72"} \quad (4.11)$$

$$P_D = P_2\frac{Y_{bc} - Y_t}{72"} \quad (4.12)$$

PA, PB, PC, and PD are the effective loads at points A, B, C, and D, respectively. The following figure shows the truck's footprint. The dual wheels for axles 2 and 3 were applied as one point load in the model.

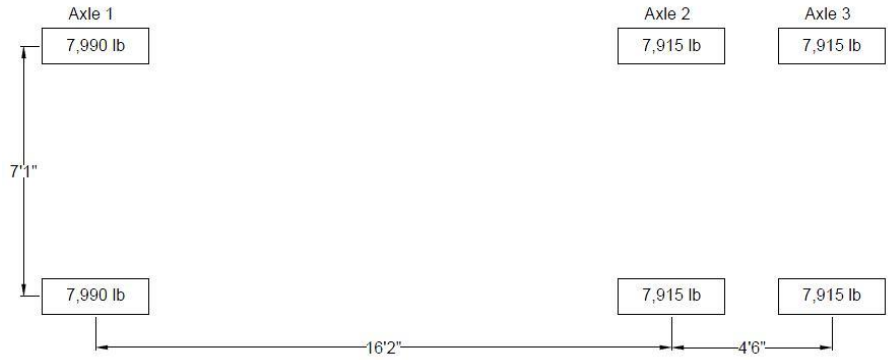

Figure 4.15 Test truck load footprint

The model results obtained were directly compared to the deflection measurements collected by BDI. After several simulation trials adjusting the axial and rotational spring stiffness, a model was obtained where most locations under different load paths had a good matching with the actual deflection measurements. Although there were some parts of the model that did not match the field results, it was determined that this model could be used further for damage analysis and the initial development of a damage index. Figure 4.16 - 4.21 show some of these comparisons.

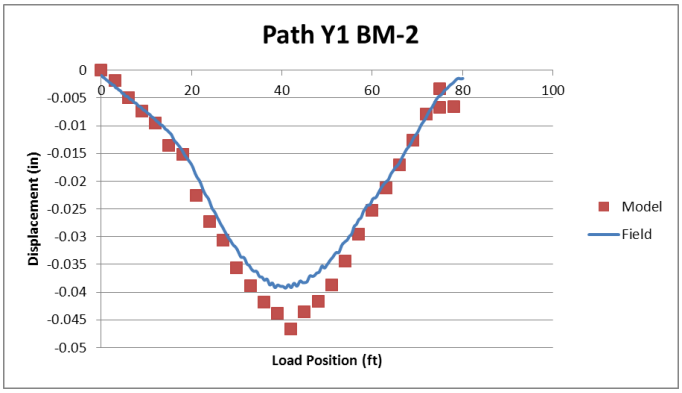

Figure 4.16 Model and measured data comparison for load path Y1 on beam 2

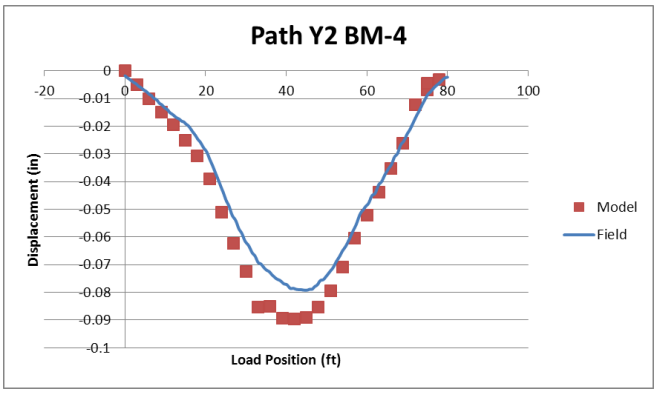

Figure 4.17 Model and measured data comparison for load path Y2 on beam 4

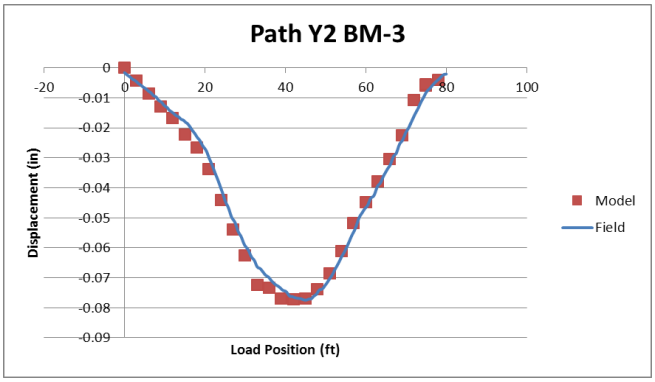

Figure 4.18 Model and measured data comparison for load path Y2 on beam 3

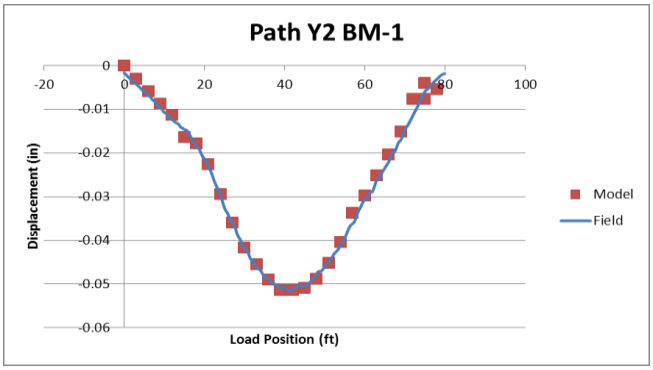

Figure 4.19 Model and measured data comparison for load path Y2 on beam 1

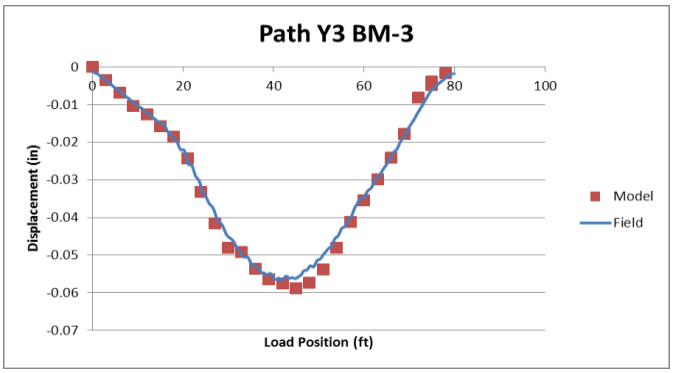

Figure 4.20 Model and field data comparison of load path Y3 on beam 3

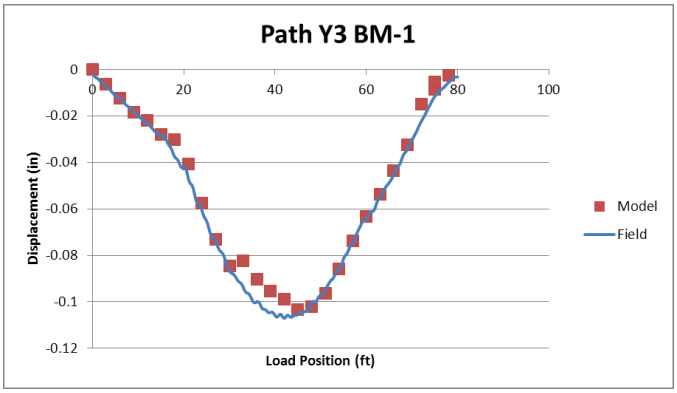

Figure 4.21 Model and field data comparison of load path Y3 on beam 1

In Figure 4.16 – 4.21, it can be seen that the deflection results from the model compare well with the measured field data. This shows that the developed model in general exhibits a similar structural response compared to the actual bridge. With this accurate model, damage simulations were conducted by reducing the Young's modulus for a section of the beam at midspan, which essentially represents a damaged section. The damaged section used was 117.0 in. (3.0 m) long centered at the midspan of the bridge. The section was reduced by three different values, 25%, 50%, and 99% for beams 1 through 4. No damage simulations were conducted for beam 5 because the model was unable to match the field data well enough. Figure 4.22 – 4.24 are examples of the effect of the reduced section for beam 1 under load path Y2.

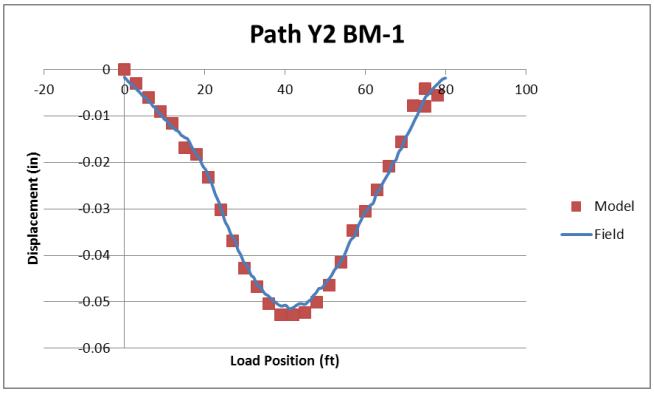

Figure 4.22 25% stiffness reduction in the damaged section at midspan

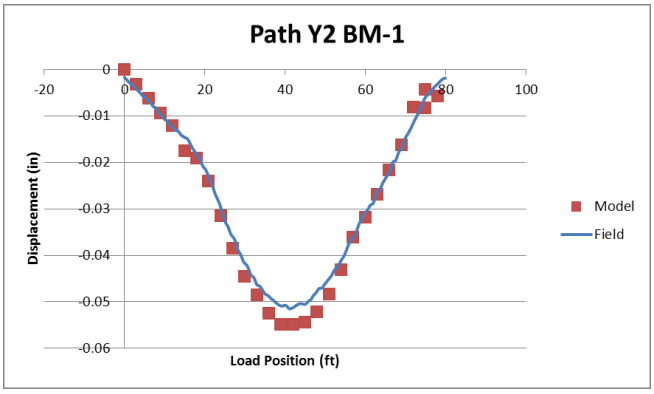

Figure 4.23 50% stiffness reduction in the damaged section at midspan

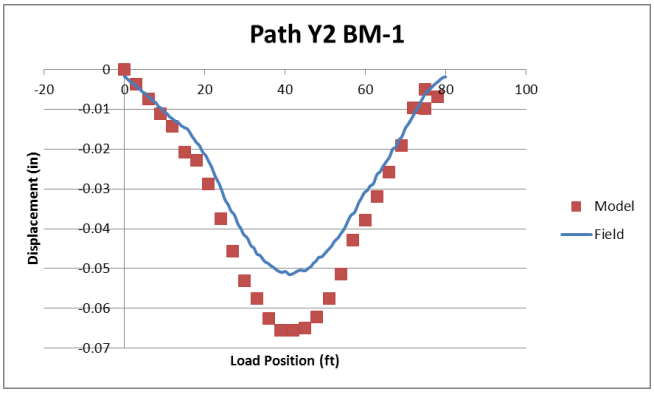

Figure 4.24 99% stiffness reduction in the damaged section at midspan

With the reduced section stiffness the deflection results from the model increased as expected. The rate of deflection generally matches the field data. The influence of the damage increases with increased reduction in section. As expected, the graph with the 99% stiffness reduction has by far the greatest effect on the deflection results. Since the longitudinal members of the model represent the deck as well as the beams, this area of the 99% stiffness reduction essentially turns the beam into two cantilever beams from each abutment.

When structural damage is present, it is postulated that the relative displacement between the two locations will begin to diverge more and more with increasing damage. This idea was originated from Phares et al. at Iowa State University (Phares et al., 2011).[43] In their project, the strain measurements of two sensors at the near field and the far field of the targeted location were compared to create a ratio. Ratios of the damaged bridges were compared with those of the undamaged bridge. It was hypothesized that difference between the ratios would be an indication of damage accumulation. In this research, the idea is extended to the deflection results and will serve to indicate damage in the structure as well as the location of the damage. It must be pointed out the comparison is not necessarily made to the undamaged bridge. Any newly accumulated damage between the bridges can be detected when the displacement ratio of these two bridges changes.

The displacement ratio is calculated by the relative displacement between two certain locations in the undamaged state along the entire load path. A ratio of the damaged over the undamaged case is then calculated at each load step and then averaged. The deviation of this ratio from unity is an indication of damage, and the highest deviation is close to the damage location. The simulated stiffness reduction level and location for each damage case are detailed in Table 4.2. Figure 4.25 shows the damage ratio results for beam 1 in damage cases 1-3. The 1&3 Y2 defines the displacement ratio between beams 1 and 3 under the truck load path Y2. Similarly, 2&4 Y1 defines the displacement ratio between beams 2 and 4 under the truck load path Y1. The data are consistent in showing that, with increased damage, the ratio diverges away from unity. It is also anticipated that beam 1 and 3 show the greatest distance from unity compared with that of the ratios between beam 2 and 4.

Table 4.2 The damage cases with different stiffness reduction levels

Damage Case	Beam	Stiffness Reduction
1	1	25%
2	1	50%
3	1	99%
4	2	25%
5	2	50%
6	2	99%
7	3	25%
8	3	50%
9	3	99%
10	4	25%
11	4	50%
12	4	99%

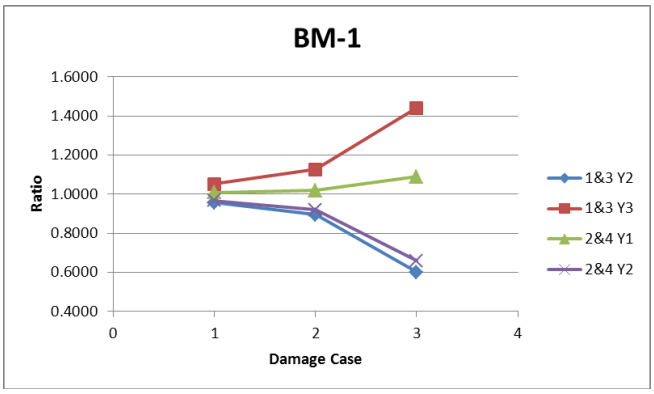

Figure 4.25 Beam 1 displacement ratio indexes for damage cases 1-3

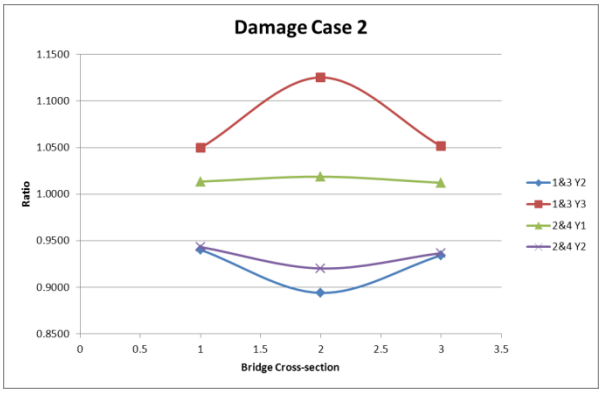

Figure 4.26 Displacement ratio indexes along bridge for Damage Case 2

Figure 4.26 shows the displacement ratios for damage case 2 along the longitudinal direction of the bridge. In the figure, at point 1 along the x-axis is the ratio of the relative displacement at section 1, which is 117.0 in. (3.0 m) from the west end of the bridge. Point 3 along the x-axis shows the ratios of the relative displacement at section 3, located 117.0 in. (3.0 m) from the east end of the bridge. The ratios at point 2 on the x-axis (midspan) are consistently farther away from unity when compared with cross-sections 1 and 3. This indicates the ratio is sensitive to damage locations and is also consistent because the values at cross-section 1 and 3 are very similar. Figure 4.27 shows similar data except for the same location with different damage cases.

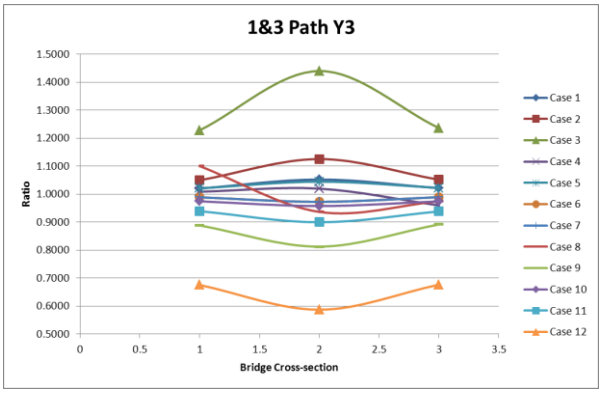

Figure 4.27 Displacement ratio indexes for Beams 1 and 3 under load path Y3 for cases 1-12

4.4 Impact/collision detection through the integration of SHM and impact/collision collection system

The same sensor deployment can be adopted to capture the location of the impact or collision events. Through the strain time measurement, the algorithm developed in Chapter 3 could be used to locate the impact/collision positions, subject to boundary condition adjustments.

4.5 Conclusions

This report discussed the development of a simple two dimensional finite element model using the "grillage method." The model was able to match well with the field test deflection data and was used to simulate the effect of structural damage on bridge responses. Based on the bridge response with damaged structural members, a damage ratio index (or displacement ratio index) is developed to quantify the level of damage and its location. The initial results show that severity of the damage and the location of damages are consistent with the variation of displacement ratio index. The same deployment of sensors could be used to locate the impact/collision position, which could serve as a history record of any infrastructure system.

5. REFERENCES

[1] Giurgiutiu, V. 2003. Lamb wave generation with piezoelectric wafer active sensors for structural health monitoring *Proceedings of SPIE* **5056** 111–122

[2] Mal, A. K., Shih, F., and Banerjee, S. 2003. Acoustic emission waveforms in composite laminates under low velocity impact. *Proceedings of SPIE* **5047** 1–12

[3] Mal, A. K., Ricci, F., Gibson, S., and Banerjee, S. 2003. Damage detection in structures from vibration and wave propagation data. *Proceedings of SPIE* **5047** 202–10

[4] Derriso, M. M. and Olson, S. E. 2005. The future role of structural health monitoring for air vehicle applications. *Proc. 5th IWSHM* ed. Chang F. K. pp. 17–25

[5] Rahani, E. K., Kundu, T., Wu, Z., and Xin, H. 2011. "Mechanical Damage Detection in Polymer Tiles by THz Radiation." *IEEE Sensors Journal* **11** 1720-5

[6] Tsutsui, H., Kawamata, A., Sanda, T., and Takeda, N. 2004. "Detection of impact damage of stiffened composite panels using embedded small-diameter optical fibers." *Smart Material and Structures* **13** 1284–90

[7] Yan, G. and Zhou, L. 2009. "Impact load identification of composite structure using genetic algorithms." *Journal of Sound and Vibration* **319** 869–84

[8] Seydel, R. and Chang, F. K. 2001. "Impact identification of stiffened composite panels: I. System development." *Smart Materials and Structures* **10** 354–69

[9] Seydel, R. and Chang, F. K. 2001. "Impact identification of stiffened composite panels: II. Implementation studies." *Smart Materials and Structures* **10** 370–9

[10] Kazemi, M. and Hematiyan, M. R. 2009. "An efficient inverse method for identification of the location and time history of an elastic impact load." *Journal of Testing and Evaluation* **37** 545-55

[11] Hajzargerbashi, T., Kundu, T., and Bland, S. 2011. "An improved algorithm for detecting point of impact in anisotropic inhomogeneous plates." *Ultrasonics* **51** 317–24

[12] Peelamedu, S. M., Ciocanel, C., and Naganathan, N. G. 2004. "Impact detection for smart automotive damage mitigation systems." *Smart Materials and Structures* **13** 990–7

[13] Xu, S., Deng, X., Tiwari, V., Sutton, M. A., Fourney, W. L., and Bretall, D. 2010. "An inverse approach for pressure load identification." *International Journal of Impact Engineering* **37** 865–77

[14] Mao, Y. M., Guo, X. L., and Zhao, Y. 2010. "Experimental study of hammer impact identification on a steel cantilever beam." *Experimental Techniques* **34** 82–5

[15] Schäfera, F. and Janovsky, R. 2007. "Impact sensor network for detection of hypervelocity impacts on spacecraft." *Acta Astronautica* **61** 901-11

[16] Chen, C., Li, Y. and Yuan, F. G. 2012. "Impact source identification in finite isotropic plates using a time-reversal method." *Smart Materials and Structures* **21** 105025-35

[17] Sekula, K., Graczykowski, C., and Holnicki-Szulc, J. 2013. “On-line impact load identification.” *Shock and Vibration* **20**, 123-141

[18] Gunawan, F. E., Homma, H., and Kanto, Y. 2006. “Two-step B-spline regularization method for solving an ill-posed problem of impact-force reconstruction.” *Journal of Sound and Vibration* **297** 200-14

[19] Park, J., Ha, S., and Chang, F. K. 2011. “Monitoring impact events using a system identification method.” *AIAA Journal* **47** 2011-21

[20] Chandrashekara, K., Okafor, A. C., and Jiang, Y. P. 1996. Estimation of contact force on composite plates using impact induced strain and neural network. *Proceedings of SPIE – The International Society for Optical Engineering* **2718** 320-30

[21] Akhavan, F., Watkins, S. E., and Chandrashekara, K. 1996 Recovery of impact contact forces of composite plates using fiber optic sensors and neural networks. *Proceedings of SPIE – The International Society for Optical Engineering* **2839** 277-88

[22] Sung, D. U., Oh, J. H., Kim, C. G., and Hong, C. S. 2000. “Impact monitoring of smart composite laminates using neural network and wavelet analysis.” *Journal of Intelligent Material System and Structures* **11** 180-90

[23] Jankowski, L. 2009. “Off-line identification of dynamic load.” *Structural and Multidisciplinary Optimization* **37** 609-623

[24] Pedersen, M. E. H. and Chipperfield, A. J. 2010. “Simplifying particle swarm optimization.” *Applied Soft Computing* **10** 618-28

[25] Trelea, I. C. 2003. “The particle swarm optimization algorithm convergence analysis and parameter selection.” *Information Processing Letters* **85** 317-25

[26] Bai, Q. 2010. “Analysis of particle swarm optimization.” *Algorithm Computer and Information Science* **3** 180-84

[27] Fontan, M., Ndiaye, A., Breysse, D., and Castéra, P. 2012. “Inverse analysis in civil engineering: Applications to identification of parameters and design of structural material using mono or multi-objective particle swarm optimization.” *Theory and New Applications of Swarm Intelligence*, edited by R. Parpinelli and H. S. Lopes.

[28] Fontan, M., Ndiaye, A., Breysse, D., Bos, F., and Fernandez, C. 2011. “Soil–structure interaction: Parameters identification using particle swarm optimization.” *Computers and Structures* **89** 1602–14

[29] Jacquelin, E., Bennani, A., and Hamelin, P. 2003. “Force Reconstruction: analysis and regularization of a deconvolution problem.” *Journal of Sound and Vibration* **265** 81-107

[30] Zhou, X. Q. and Law, S. S. 2002. “Moving loads identification through regularization.” *Journal of Engineering Mechanics* **128** 989-1000

[31] Doyle, J. F. 1993. “Force identification from dynamic responses of a biomaterial beam.” *Experimental Mechanics* **33** 64-9

[32] Han, S. L. and Kinoshita, T. 2012. “Investigation of stochastic inverse method to estimate an external force: Applications to a wave-structures interaction.” *Mathematical Problems in Engineering* **2012** 25 pages

[33] Ma, C. K. and Ho, C. C. 2004. “An inverse method for the estimation of input forces acting on non-linear structural systems.” *Journal of Sound and Vibration* **275** 953–71

[34] Liu, J., Han, X., Jiang, C., Ning, H. M. and Bai, Y. C. 2011. “Dynamic load identification for uncertain structures based on interval analysis and regularization method.” *International Journal of Computational Methods* **8** 667–83

[35] Jiang, C., Han, X., Guan, F. J., and Li, Y. H. 2007. “An uncertain structural optimization method based on nonlinear interval number programming and interval analysis method.” *Engineering Structures* **29** 3168–77

[36] Qiu, Z. and Wang, X. 2003. “Comparison of dynamic response of structures with uncertain-but-bounded parameters using non-probabilistic interval analysis method and probabilistic approach.” *International Journal of Solids and Structures* **40** 5423–39

[37] Whitney, J. M. and Pagano, N. J. 1970. “Shear deformation in heterogeneous anisotropic plates.” *Journal of Applied Mechanics* **37** 1031-6

[38] Carvalho, A. and Soares, C. G. 1996. “Dynamic response of rectangular plates of composite materials subjected to impact loads.” *Composite Structures* **34** 55-63

[39] Dobyns, A. L. 1981. “Analysis of simply-supported orthotropic plates subject to static and dynamic loads.” *The American Institute of Aeronautics and Astronautics (AIAA)* **19** 642-50

[40] Ahmari, S. and Yang, M. 2013. “Impact location and load identification through inverse analysis with bounded uncertain measurements.” *Smart Materials and Structures* 22 doi:10.1088/0964-1726/22/8/085024

[41] Bridge Diagnostics, Inc., July 2012, “Field testing and load rating report: Bridge 09-125-16.0 over Rush River Cass County, ND.”

[42] Jaeger, L. D. and Bakht, B., 1982, “The grillage analogy in bridge analysis,” *Can. J. Civ. Eng.*, 9, 224-235

[43] Phares, B. M., Wipf, T.F, Lu, P., Greimann, L., Pohlkamp, M., January 2011, “An Experimental Validation of a Statistical-Based Damage-Detection Approach,” Final Report, Institute for Transportation, Iowa State University.